PHOTOACOUSTIC AND THERMOACOUSTIC TOMOGRAPHY:

SYSTEM DEVELOPMENT FOR BIOMEDICAL APPLICATIONS

A Dissertation

by

GENG KU

Submitted to the Office of Graduate Studies of
Texas A&M University
in partial fulfillment of the requirements for the degree of

DOCTOR OF PHILOSOPHY

December 2004

Major Subject: Biomedical Engineering

PHOTOACOUSTIC AND THERMOACOUSTIC TOMOGRAPHY:

SYSTEM DEVELOPMENT FOR BIOMEDICAL APPLICATIONS

A Dissertation

by

GENG KU

Submitted to Texas A&M University
in partial fulfillment of the requirements
for the degree of

DOCTOR OF PHILOSOPHY

Approved as to style and content by:

Lihong Wang (Chair of Committee)	Hsin-i Wu (Member)
Gerard L. Coté (Member)	Georghe Stoica (Member)
William Hyman (Head of Department)	

December 2004

Major Subject: Biomedical Engineering

ABSTRACT

Photoacoustic and Thermoacoustic Tomography:

System Development for Biomedical Applications. (December 2004)

Geng Ku, B.S., Huazhong University of Science and Technology;

M.S., Huazhong University of Science and Technology

Chair of Advisory Committee: Dr. Lihong V. Wang

Photoacoustic tomography (PAT), as well as thermoacoustic tomography (TAT), utilize electromagnetic radiation in its visible, near infrared, microwave, and radiofrequency forms, respectively, to induce acoustic waves in biological tissues for imaging purposes. Combining the advantages of both the high image contrast that results from electromagnetic absorption and the high resolution of ultrasound imaging, these new imaging modalities could be the next successful imaging techniques in biomedical applications. Basic research on PAT and TAT, and the relevant physics, is presented in Chapter I. In Chapter II, we investigate the imaging mechanisms of TAT in terms of signal generation, propagation and detection. We present a theoretical analysis as well as simulations of such imaging characteristics as contrast and resolution, accompanied by experimental results from phantom and tissue samples. In Chapter III, we discuss the further application of TAT to the imaging of biological tissues. The microwave absorption difference in normal and cancerous breast tissues, as well as its influence on thermoacoustic wave generation and the resulting transducer response, is investigated

over a wide range of electromagnetic frequencies and depths of tumor locations. In Chapter IV, we describe the mechanism of PAT and the algorithm used for image reconstruction. Because of the broad bandwidth of the laser-induced ultrasonic waves and the limited bandwidth of the single transducer, multiple ultrasonic transducers, each with a different central frequency, are employed for simultaneous detection. Chapter V further demonstrates PAT's ability to image vascular structures in biological tissue based on blood's strong light absorption capability. The photoacoustic images of rat brain tumors in this study clearly reveal the angiogenesis that is associated with tumors. In Chapter VI, we report on further developing PAT to image deeply embedded optical heterogeneity in biological tissues. The improved imaging ability is attributed to better penetration by NIR light, the use of the optical contrast agent ICG (indocyanine green) and a new detection scheme of a circular scanning configuration. Deep penetrating PAT, which is based on a tissue's intrinsic contrast using laser light of 532 nm green light and 1.06 μm near infrared light, is also presented.

This dissertation is dedicated

to

My father, Guihua Ku, and my mother, Jufeng Lu,

My wife, Haifang Wang, and my daughter, Tianxin Ku.

ACKNOWLEDGEMENTS

I would like to express my appreciation to Dr. Lihong Wang for his help and guidance throughout my years of research in the Optical Imaging Laboratory. Each of my publications contains his valuable contributions. His broad knowledge and acute insight have guided me all through this research.

I would like to thank Dr. George Stoica for his kindly help and support with the animal experiments. His broad knowledge in biological areas has always provided important support for my research..

I would like to express my gratitude to my advisory committee members, Dr. Hsin-i Wu and Dr. Gerard L. Coté.

I'd also like to thank Xueding Wang, Minghua Xu, Xueyi Xie, Jun Li, Xiao Xu, Sava Sakadzic, Yuan Xu, Shuliang Jiao, Gang Yao, Dazhi Feng, Hao Zhang, and Dr. Maslov for their assistance and contributions to my work.

TABLE OF CONTENTS

Page

Page

CHAPTER

Page

LIST OF FIGURES

Page

Page

Page

Page

Page

LIST OF TABLES

Page

CHAPTER I

INTRODUCTION

A. TOMOGRAPHY BASED ON ELECTROMAGNETIC ENERGY INDUCED ACOUSTIC WAVE

The absorption of electromagnetic energy causes thermal expansion and induces acoustic waves. This effect was first discovered in 1880, referred to as photoacoustic (PA) effect which was induced by light stimulation.[1] Since the first invention of working laser based on ruby in May 16th, 1960 in Hughes Research Laboratories, researches on PA effect have intensified and many technologies have been developed to been applied in physics, chemistry, biology.[2-12] In biomedical engineering, PA signal can be utilized to image biological tissues. In the Optical Imaging Lab (OIL), our research focus is stressed on revealing the biological tissue structures from PA effect. A wide spectrum of the electromagnetic radiation, including the visible range, can be used to stimulate acoustic waves in biological tissues. Because of the distinct absorption and penetration properties tissues for different wavelengths, the electromagnetic radiation could be employed for different imaging applications.[13-16] In OIL, we began this tomography research by investigation of microwave induced acoustic wave in biomedical tissues, which is referred to as thermoacoustic tomography (TAT); and developed it into photoacoustic tomography (PAT) by replacing microwave pulse with

---

This dissertation follows the style of *Optics Letters*.

laser pulse. Both microwave and visible or near infrared (NIR) laser light are non-ioning radiation and safe for biomedical applications. In this work, the term "electromagnetic energy induced acoustic tomography" refers to tomography that use any kind of electromagnetic radiation as stimulating energy; while TAT refers to one that use electromagnetic radiation in microwave band and PAT for visible and NIR light.

The motivation of EEIAT is to combine the resolution advantages of ultrasound and the contrast advantages of the electromagnetic radiation in biological tissues. Pure ultrasound imaging can provide better resolution than optical imaging in depths greater than ~1 mm, since ultrasound scattering is 2–3 orders of magnitude weaker than optical scattering in biological tissues.[17,18] However, because the ultrasound imaging is based on the detection of mechanical property differences in biological tissues, it is not sensitive to early stage tumors. Moreover, it cannot image either oxygen saturation or hemoglobin concentration. On the other hand, pure RF imaging cannot provide good spatial resolution because of its long wavelength.[19] Operating in the 500–900 MHz frequencies, RF imaging can only provide a spatial resolution of ~1 cm.[20] In PA imaging, the spatial resolution and the maximum imaging depth are scaleable with the detected ultrasonic bandwidth. Generally, the induced acoustic signal is rather wide, so the ultrasonic detection bandwidth determines the image resolution. For example, a MHz ultrasonic transducer and its corresponding electronics can provide millimeter spatial resolution.

B. ELECTROMAGNETIC WAVE PROPAGATION AND ABSORPTION IN TISSUES

Within the electromagnetic wave spectrum, the ultraviolet and sub-ultraviolet wavelength radiation have high photon energy which is ionizing for biomedical molecules, therefore, are suitable for human subjects. On the other hand, the absorption of the electromagnetic radiation in biological tissues gets smaller with lower frequency in the RF range and the induced acoustic signal becomes too weak to provide decent signal to noise ratio (SNR). So that for imaging purpose in biomedical, the excitation sources usually come from radiofrequency,[21] microwave,[22] visible light,[23] and NIR light.[24] Another important property of the electromagnetic wave and biological tissue interaction is the propagation of the EM wave inside the tissue, which can be characterized by the penetration depth, as defined by the inverse of the effective attenuation coefficient. The EM radiations in radiofrequency, microwave and visible light range have varying penetration depths, which determine their different application areas.

1. Radiofrequency properties

The radiofrequency properties of biological tissues are related to their electrical properties. There are some inorganic ions, anions and cations and some molecules present electrical dipoles, such as water and some amino acids, proteins.[25,26] The two dominant properties that affect the degree of RF absorption are ionic conductivity and the vibrational energy levels of the dipolar molecules of water and proteins in biological tissues. The absorption of tissue is determined by its molecular structures and is

electromagnetic frequency dependent. In radiofrequency and microwave band, a small increase in ionic conductivity or water content in tissue can produce a significant increase in absorption in tissues. It is believed that the ionic conductivity and/or water content in cancerous tissue are higher than in normal tissue due to an increased concentration of blood and proteins. These increases are the result of angiogenesis in rapidly growing tumors.

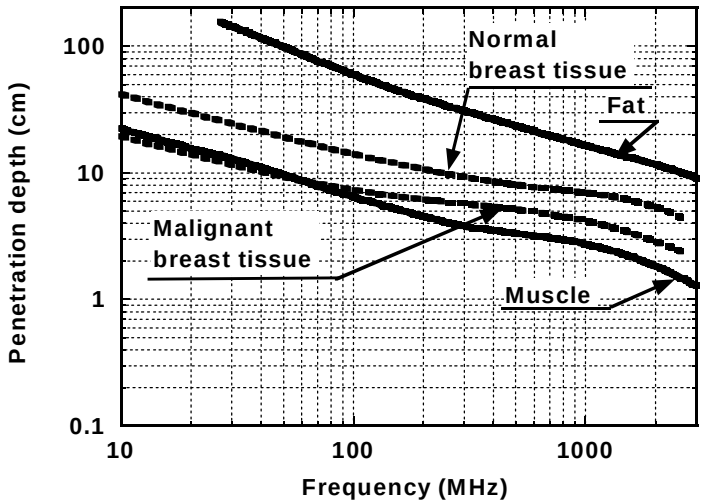

Figure 1-1. Penetration depths of various biological tissues versus microwave frequency.

The complex conductivity σ^* or the complex permittivity ε^* can be used to describe a dielectric medium's electrical property. They are defined as $\sigma^* = \sigma + j\omega\varepsilon'\varepsilon_0$ and $\varepsilon^* = \varepsilon'\varepsilon_0 + \sigma/(j\omega)$, where σ is the conductivity (S/m); ε' is the relative permittivity (dimensionless); ε_0 = 8.85 pF/m of vacuum, ω is the angular frequency of electromagnetic wave. The attenuation of the electromagnetic wave in

tissue is determined by the permittivity and conductivity, and then the 1/e penetration depth of the field is $\delta = c_0 /(2\pi f \,\mathrm{Im}\sqrt{\varepsilon^* / \varepsilon_0})$, where Re and Im represent the real and imaginary parts, respectively, and c_0 is the velocity of the electromagnetic wave in vacuum.

In figure 1-1, it is shown that the electromagnetic wave in frequency range from 100 MHz to 3 GHz, can transmit through biomedical tissues. The penetration depth is equal to the reciprocal of the absorption coefficient because the absorption is the main cause of attenuation. The absorption coefficients in fat (low water content) and muscle (high water content) are about 0.1 and 1 cm^{-1} at 3 GHz, respectively, and about 0.03 and 0.3 cm^{-1} at 300 MHz, respectively.

2. Optical properties

Visible and NIR light are the electromagnetic waves whose wavelength range from 400 to 700 nm and from 700 to 1400 nm, respectively. The absorption of the optical radiation in biological tissue is related to the molecular constituents of tissues and their electronic and/or vibrational structures. So that the optical absorption properties reveal architectural changes in biological tissue at the cellular and sub-cellular levels and can be used to quantify angiogenesis and hyper-metabolism. Figure 1-2 shows the optical absorptions in some biological tissues.[27]

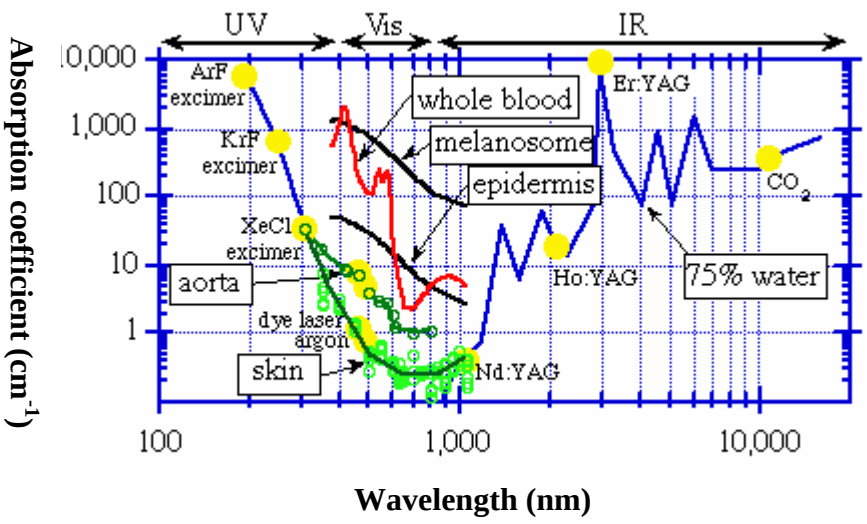

Figure 1-2. The primary absorption spectra of biological tissues and the absorption coefficients at some typical laser wavelengths.[27]

A notable characteristic of tissue's optical property is the strong scattering, which is negligible in RF and microwave range. The effective scattering coefficient is described by $\mu_s' = \mu_s(1-g)$, where μ_s and g are the scattering coefficient and the anisotropy factor, respectively. Typically $\mu_s \sim 100$ cm^{-1} and $g \sim 0.9$ in the visible to near-IR region.[18] Because of scattering, the penetration depth is not only depended on absorption alone, but also scattering. The penetration depth δ of light equals the reciprocal of the effective attenuation coefficient as $\mu_{eff} = \sqrt{3\mu_a(\mu_a + \mu_s')}$. There are two optical windows that allow light to penetrate relatively deep into biological tissues with less attenuation. One lies between 600 and 1300 nm, which is of most interested because there are many laser source provide the light at this range. Another window is between 1600 to 1850 nm (in the mid-IR range from 1400 to 3000 nm).

3. Ultrasonic properties

In the low frequency range (<10MHz), ultrasound has the low scattering and deep penetration in soft tissues.[28] The total attenuation results from the combined losses due to absorption and scattering, while the scatter component accounts for about 10–15% of the total attenuation. The attenuation coefficient in tissues varies with temperature and ultrasound frequency. Its frequency dependency can be represented by the expression $\mu = a \cdot f^{b}$, where *a*, *b* are constants and *f* is the frequency of ultrasound.[17] A mean value of ultrasound attenuation equals ~0.6 dB cm^{-1} MHz^{-1} for soft tissues.[28] The attenuation increases with frequency, so the distance over which useful levels of energy can be propagated becomes less as the frequency is increased. Typically, 3 MHz is the maximum frequency for a 150-mm penetration.[28] However, in the high frequency range, both scattering and absorption increase tremendously, and penetration depth decrease remarkably. For higher frequency, the attenuation also depends strongly on the other characteristics of the tissue, such as strain and tissue type. This can be illustrated by the following data. The ultrasonic attenuation coefficient for human skin is linearly dependent on frequency in the range from 17 MHz to 35 MHz, which is 5 dB/mm to 10 dB/mm at zero strain and changed to 2.2 dB/mm to 5.2 dB/mm at 47% strain. The penetration depth is 1.74 mm to 0.87 mm and 3.95 mm to 1.67 mm correspondingly.[29]

For skin, the attenuation can be expected to be in the range of 50 – 125 dB/mm for frequency of 100 – 200 MHz range, with $a \cdot f^{1.3}$ dependence.[30] From 20 MHz to 100 MHz ultrasound, the attenuation coefficient for femoral artery is in the range of 2.8

dB/mm to 17.5 dB/mm,[31] showing in the Table 1-1, Table 1-2, and Table 1-3, respectively.

Table 1-1. Ultrasonic attenuation of skin at the frequency of 17 MHz and 35 MHz

Ultrasonic frequency (MHz)	17 MHz	35 MHz
Attenuation Coefficient (dB/mm) -- 0 Strain; [] – 47% Strain	5 [2.2]	10 [5.2]
Penetration Depth (mm) -- 0 Strain; [] – 47% Strain	1.74 [3.95]	0.87 [1.67]

Table 1-2. Ultrasonic attenuation of skin at the frequency of 100 MHz and 200 MHz

Ultrasonic frequency (MHz)	100	200
Attenuation Coefficient (dB/mm)	50	125
Penetration Depth (mm)	0.174	0.070

Table 1-3. Ultrasonic attenuation of artery

Ultrasonic frequency (MHz)	20	100
Attenuation Coefficient (dB/mm)	2.8	17.5
Penetration Depth (mm)	3.10	0.496

C. INDUCED ACOUSTIC WAVE MECHANISM

Upon absorption in tissue, the electromagnetic energy is converted into heat, which is then converted into mechanical energy by thermoelastic expansion as well as the pressure propagation. The local pressure rises immediately after the heat is built up. The temperature rise as a result of the energy deposition inside the biological tissue can be estimated as follows:

For microwave peak power of 10 kW, pulse width of 0.5 microsecond, the power density is 5 mJ/(7.5 cm x 0.5 cm) = 1.33 mJ/cm^2.

$$E_a = cm\Delta t$$

$$\Delta t = \frac{E_a}{c \cdot m} = \frac{\mu_a \cdot I \cdot dV}{c \cdot \rho \cdot \cdot dV} = \frac{\mu_a \cdot I}{c \cdot \rho \cdot} = \frac{1(cm^{-1}) \cdot 1.33(mJ/cm^2)}{4(Jg^{-1}K^{-1}) \cdot 1.06(g/cm^3)} = 0.3(mK) \approx 300(\mu K)$$

$$\Delta P = \Gamma E_a = \Gamma \mu_a I$$

$$\Delta P = 0.24 * 200(cm^{-1}) \cdot 14.6(mJ/cm^2) = 700(mJ/cm^3) = 700000(Pa) = 7(bar)$$

$$(1\frac{J}{m^3} = \frac{Nm}{m^3} = \frac{N}{m^2} = 1P_a, 1\frac{mJ}{m^3} = 10^3 P_a)$$

$\mu_a \approx 1(cm^{-1})$: Absorption coefficient of a tissue object

$I = 1.33(mJ/cm^2)$: Microwave power density.

$c = 4(Jg^{-1}K^{-1})$: Heat capacity of a tissue

$\rho = 1.06(g/cm^3)$: Mass density of whole blood, human.

The temperature and pressure rise are about 0.3 mini degree and 1.46 mini bar, respectively.

For the photoacoustic tomography under the exciting by a Q-switched laser pulse of 532 nm wavelength:

$$E_a = cm\Delta t$$

$$\Delta t = \frac{E_a}{c \cdot m} = \frac{\mu_a \cdot I \cdot dV}{c \cdot \rho \cdot \cdot dV} = \frac{\mu_a \cdot I}{c \cdot \rho \cdot} = \frac{200(cm^{-1}) \cdot 20(mJ/cm^2)}{3.84(Jg^{-1}K^{-1}) \cdot 1.06(g/cm^3)} = 0.98(K) \approx 1(K)$$

$\Delta p = 1.1 \times 20(mJ/cm^2) = 22(mbar)$

$\mu_a \approx 200(cm^{-1})$: Absorption coefficient of whole blood, human

$I = 20(mJ/cm^2)$: Maximum permissible exposure (MPE) of green light. ANSI Standard Z 136.1-2000.

$c = 3.84(Jg^{-1}K^{-1})$: Specific heat capacity for whole blood, human.

$\rho = 1.06(g/cm^3)$: Mass density of whole blood, human.

The temperature and pressure rise are about one degree and 22 mini bar, respectively.

For most biology soft tissues, the thermal diffusion effect on the PA signal is usually negligible as long as the electromagnetic energy is deposited in the sample within a relatively short time. Short excitation pulses within microseconds meet the requirement for thermal confinement and stress confinement. Therefore, the efficiency of PA generation is high. The absorption of the pulse energy, the thermal diffusion during the pulse period can be estimated by the thermal diffusion length:[2] $\delta_T = 2\sqrt{D_T \tau_p}$, where τ_p is the pulse duration and D_T is the thermal diffusivity of the sample. Thermal diffusivity for most soft tissues is $D_T \sim 1.4 \times 10^{-3} \text{cm}^2/\text{s} = 0.14\ \mu\text{m}^2/\mu\text{s}$ [17]. For example, the longest excitation pulse employed in TAT and PAT are 1 μs for microwave and 15 ns for laser, the corresponding τ_p are 1 μs and 0.015 μs, so δ_T are 0.37 μm and 0.05 μm, which are typically much less than the spatial resolution of TAT and PAT imaging system. In our

applications, the real absorbing objects or the characteristic heating length L_p defined by the penetration depth of the stimulating electromagnetic wave is much bigger than the thermal diffusion size.

The induced acoustic waves spread in the medium along all directions, which is described by wave equation. For simplicity, the inhomogeneity of acoustic speed in soft tissues is usually neglected in evaluating the acoustic wave propagation. The speed of sound is relatively constant at 1.5 mm/μs with a small variation of less than 5% in most soft tissues.[17,28]

Following are some fundamental equations and typical solution related to the acoustic wave propagation. In response to a heat source $H(\mathbf{r},t)$, without considering thermal diffusion and kinematical viscosity, the pressure $p(\mathbf{r},t)$ at position **r** and time *t* in an acoustically homogeneous liquid-like medium obeys the following wave equation:[2,12,32]

$$\nabla^2 p(\mathbf{r},t) - \frac{1}{c^2}\frac{\partial^2}{\partial t^2} p(\mathbf{r},t) = -\frac{\beta}{C_p}\frac{\partial}{\partial t} H(\mathbf{r},t) \qquad (1\text{-}1)$$

where $p(\mathbf{r},t)$ is the thermoacoustic pressure at the position **r** and time *t*, c is the speed of sound; β is the isobaric volume expansion coefficient, C_p is the heat capacity, and $H(\mathbf{r},t)$ is the heating function defined as the thermal energy deposited by the electromagnetic radiation per unit time and per unit volume.

The solution, which is based on Green's function, can be found in physics or mathematics literature.[33–36] In general, the solution to Eq. (1.1) in the time domain can be expressed by

$$p(\mathbf{r},t)=\frac{\beta}{4\pi C_p}\iiint\frac{d^3r'}{|\mathbf{r}-\mathbf{r}'|}\frac{\partial H(\mathbf{r}',t')}{\partial t'}\bigg|_{t'=t-\frac{|\mathbf{r}-\mathbf{r}'|}{c}} \tag{1-2}$$

The heating function can be written as the product of a spatial absorption function of objects and a temporal illumination function for stimulating:

$$H(\mathbf{r},t)=A(\mathbf{r})I(t) \tag{1-3}$$

Particularly, if $I(t)=\delta(t)$, the initial induced pressure at position $\mathbf{r}$ equals $p_0(\mathbf{r})=\Gamma(\mathbf{r})A(\mathbf{r})$ [37], where $\Gamma(\mathbf{r})$ is the Grüneisen parameter equal to $c^2\beta/C_p$.

Thermal-confinement condition is assumed, since the acoustic transit time across the acoustic source is less than the heat conduction time. The solution to the three-dimensional wave equation under the zero-initial-value conditions $p(0,\mathbf{r})=0$ and $\frac{\partial}{\partial t}p(0,\mathbf{r})=0$ can be expressed as an integral:

$$p(\mathbf{r},t)=\frac{\beta}{4\pi C_p}\iiint\frac{1}{|\mathbf{r}-\mathbf{r}'|}\frac{\partial H(\mathbf{r}',t')}{\partial t'}d\mathbf{r}'. \tag{1-4}$$

The integration is carried out over a sphere with a radius of $v_s t$ centered at $\mathbf{r}$, and $\mathbf{r}'$ is the position inside the sphere where microwave is absorbed and acoustic signal is generated. In the integration, the heating function is not taken at time t but at an earlier

time $t' = t - |\mathbf{r} - \mathbf{r}'| / v_s$; therefore, the integration function is also called retarded potential.[38] Analytic solutions can be obtained for simple geometric structures such as an infinite layer, a sphere, and a cylinder under delta heating, where the heating function is a delta function in time.[39]

For more general non-thermal-confined cases where heat transfer in the medium cannot be neglected, the following heat conduction equation must be taken into account in the pressure calculation:

$$\rho C_p \frac{\partial T(\mathbf{r},t)}{\partial t} = k\nabla^2 T(\mathbf{r},t) + H(\mathbf{r},t), \qquad (1\text{-}5)$$

where ρ is the medium density, k is the thermal conductivity, and $T(\mathbf{r},t)$ is the temperature distribution in the microwave-illuminated volume. The thermoacoustic pressure is:

$$p(\mathbf{r},t) = \frac{\beta}{4\pi C_p} \iiint \frac{1}{|\mathbf{r} - \mathbf{r}'|} \left[\frac{\partial H(\mathbf{r}',t')}{\partial t'} + k\nabla^2 \frac{\partial T(\mathbf{r}',t)}{\partial t'} \right] d\mathbf{r}' . \qquad (1\text{-}6)$$

The integration involves the heat transferred from the surrounding medium as well as the heat generated from to the locally absorbed electromagnetic energy.

CHAPTER II

SCANNING MICROWAVE-INDUCED THERMOACOUSTIC TOMOGRAPHY: SIGNAL, RESOLUTION, AND CONTRAST

A. THERMOACOUSTIC SIGNALS GENERATED IN BIOLOGICAL TISSUES

Purely-microwave imaging of biological tissues has been investigated for a number of years.[40-44] The advantages of microwave imaging include the use of non-ionizing radiation and relatively good imaging contrast. However, purely-microwave imaging has had difficulties in multi-channel detection of microwave without cross coupling, in reconstruction algorithms, and especially in achieving good spatial resolution because of the strong diffraction of microwaves. Purely-ultrasound imaging (ultrasonography), an established medical imaging modality, can yield good spatial resolution but has poor contrast for early-stage tumors. Microwave-induced thermoacoustics can potentially bridge the gap and fuse the advantages of the two imaging modalities.

In microwave-induced thermoacoustics, microwave pulses generate acoustic waves in electromagnetically lossy media. This phenomenon was known as microwave-auditory or microwave-hearing effect in the early years of last contrary.[45] Microwave-induced thermoacoustics were used to quantify physical parameters in media such as the power density and the concentration of a given substance.[46-48] Several investigators employed microwave-induced thermoacoustics in the 1980s for imaging of biological tissues.[49-54] However, these early works did not produce any tomographic or depth-

resolved images. Recently, images of biological tissues were computationally reconstructed based on microwave-induced thermoacoustics.[21,55] This approach requires measurements of a large amount of data around the tissue and post-processing computation. Our group explored scanning microwave-induced thermoacoustic tomography.[22,56] Our approach is similar to the conventional ultrasonic B-scan except that the ultrasound is produced internally inside the tissue by microwave pulses. This scanning approach can potentially provide real-time imaging and image co-registration with ultrasonic B-scan.

Microwave-induced thermoacoustic imaging is based on the detection of the thermoacoustic signals generated by microwave radiation in the samples. Microwave pulses are used to irradiate the samples. Absorbed microwave energy causes thermoelastic expansion, which radiates acoustic waves, termed thermoacoustic waves. An ultrasonic transducer detects the time-resolved thermoacoustic signals. If optical radiation instead of microwave radiation is used, this thermoacoustic phenomenon is better known as photoacoustics. Microwave-induced thermoacoustic imaging shares similar principles with its optical counterpart.[22,24,57−60] However, microwave-induced thermoacoustic imaging may find unique applications in medical imaging because microwave radiation provides a deeper penetration depth in biological tissues than light and has different contrast mechanisms.

In our scanning microwave-induced thermoacoustic tomography, the ultrasonic transducer measured the time-of-arrival signals of the thermoacoustic waves. The distance between the thermoacoustic source and the transducer was calculated by

multiplying the time of arrival with the speed of sound in the medium. Therefore, a time-domain signal was converted into a one-dimensional image along the acoustic axis (*z* axis), which is similar to an ultrasonic A-scan image. Scanning the sample along the *x* or *y* axis and combining the multiple one-dimensional images yielded a two-dimensional cross-sectional image of the sample in the *x*-*z* or *y*-*z* plane.

B. EXPERIMENTAL SETUP AND METHODS

The experimental setup used for this study is shown in Fig. 2-1. A Cartesian coordinate system was set up for reference. The *z* axis was along the acoustic axis pointing upward. The *x* axis was perpendicular to the drawing plane and pointed outward. The *y* axis was in the drawing plane pointing to the right. A 3-GHz microwave generator transmitted microwave pulses. The peak power was estimated to be 2 kW. The pulse width was modified to 0.5 μs. A function generator (DS345, Stanford Research System) was employed to trigger the microwave generator, control its pulse repetition frequency, and synchronize the oscilloscope sampling. Microwave energy was delivered by a rectangular waveguide with a cross section of 72 mm X 34 mm. The object to be imaged was placed on a plastic stand inside a plexiglass container filled with mineral oil. The container was fixed on a two-dimensional *x*-*y* translation stage (MD2, Arrick Robotics). A personal computer controlled the two stepper motors to drive the translation stage in the *x* and *y* directions. Both mineral oil and plexiglass have a small absorption coefficient for microwaves. Mineral oil also provides good acoustic coupling. An ultrasonic transducer was immersed in the mineral oil facing the microwave waveguide. The transducer was connected to a pulse amplifier. The amplified signal was

recorded and averaged 100 times by an oscilloscope (TDS-640A, Tektronix) and then transferred to a personal computer for imaging.

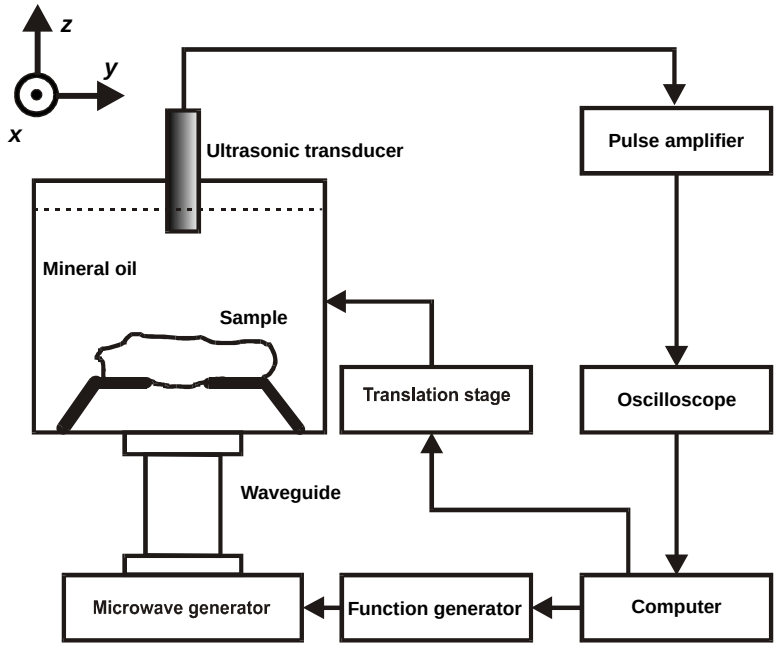

Figure 2-1. Experimental setup for scanning thermoacoustic tomography.

Two ultrasonic transducers were used in this study. For the first one (V314, Panametrics), the central frequency of the ultrasonic transducer was 1 MHz, the bandwidth was 0.6 MHz, the diameter was 1.9 cm, and the focal length at 1 MHz was 2.5 cm. For the second one (V384, Panametrics), the central frequency was 3.5 MHz, the bandwidth was 2.5 MHz, the diameter was 0.64 cm, and the focal length at 3.5 MHz was 1.8 cm. Unless otherwise stated, the first ultrasonic transducer was used to obtained the results presented here.

In our scanning microwave-induced thermoacoustic tomography, the ultrasonic transducer measured the time-of-arrival signals of the thermoacoustic waves. The

distance between the thermoacoustic source and the transducer was calculated by multiplying the time of arrival with the speed of sound in the medium. Therefore, a time-domain signal was converted into a one-dimensional image along the acoustic axis (*z* axis), which is similar to an ultrasonic A-scan image. Scanning the sample along the *x* or *y* axis and combining the multiple one-dimensional images yielded a two-dimensional cross-sectional image of the sample in the *x*-*z* or *y*-*z* plane.

C. THERMOACOUSTIC SIGNAL SIMULATION AND TEST RESULT

1. In time domain

Continuing to the solution of wave equation and analysis in chapter I, part C, for a slab with a thickness *d* under delta heating, the impulse-response pressure is

$$p_1(z,t) = \frac{\beta v_s^{\,2}}{2C_p} u(z - v_s t), \qquad (2\text{-}1)$$

where $u(z - v_s t)$ is defined as a function that is unity when $0 \le (z - v_s t) \le d$ and zero otherwise. The impulse response is a traveling square wave as shown in Fig. 2(a) for a 4.8-mm gel slab if the microwave attenuation across the slab is negligible. Because the propagation speed of electromagnetic wave is much greater than the speed of sound, the sample volume illuminated by microwave pulses radiates acoustic waves simultaneously.

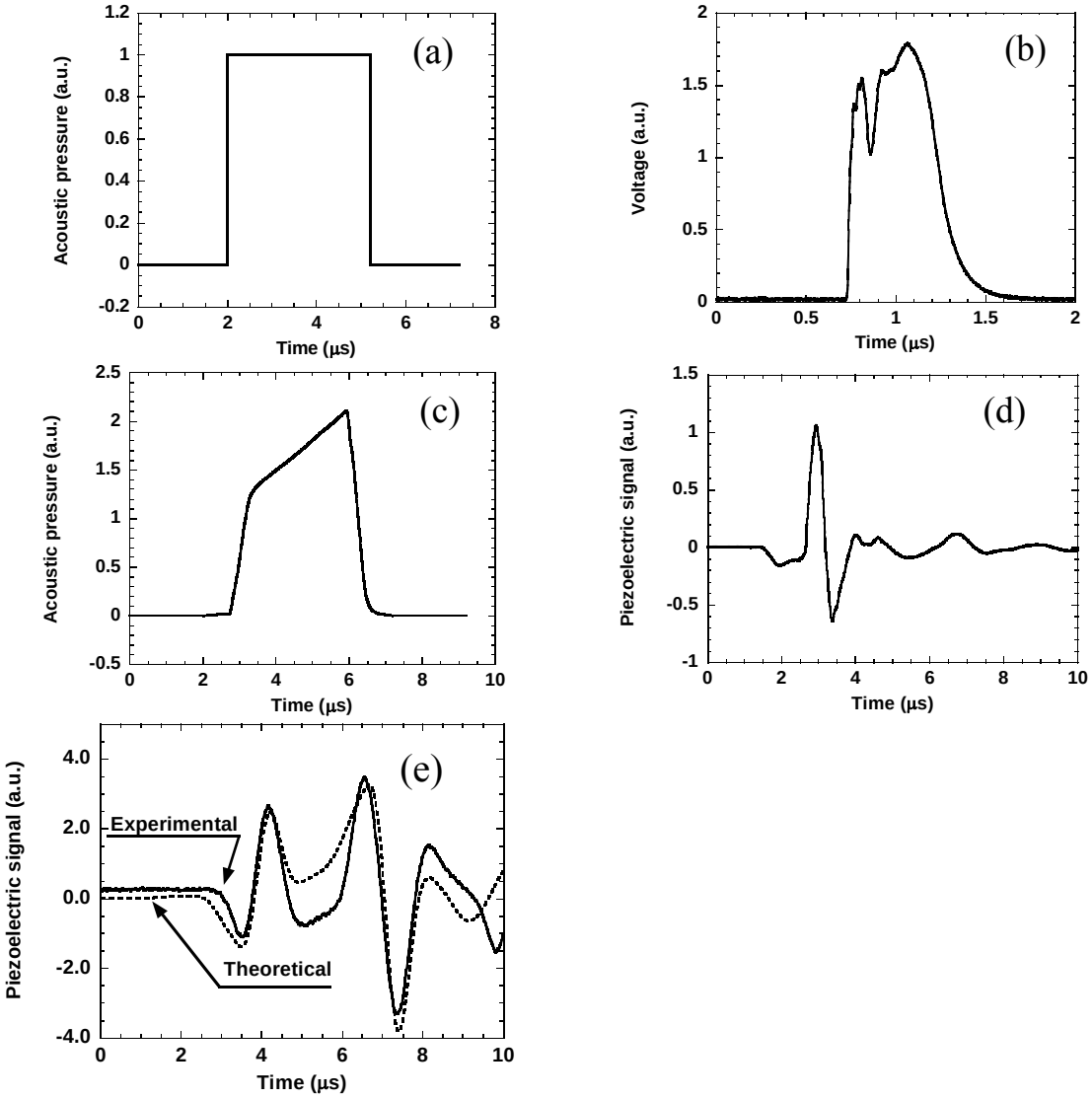

Figure 2-2. Simulation of the piezo-electric signal in response to the microwave-induced thermoacoustic signal from a 4.8-mm thick gel slab. (a) Thermoacoustic signal in a slab induced by an ideal microwave impulse; (b) Temporal profile of the microwave pulses used in the experiment; (c) Thermoacoustic signal in a slab induced by the microwave pulses used in the experiment; (d) Piezo-electric impulse response of the ultrasonic transducer; (e) Experimental and simulated piezo-electric outputs of the ultrasonic transducer in response to the thermoacoustic signals.

The heating function in one-dimensional lossy media may be expressed as $H(z,t) = \alpha e^{-\alpha z} s(t)$, where α is the microwave absorption coefficient, and *s(t)* is the temporal profile of the microwave pulse. Figure 2(b) shows the temporal profile of the microwave pulses used in our experiment.

The thermoacoustic pressure induced by the microwave pulses can be derived by the following convolution:

$$p(z,t) = \int p_1(z,\tau) H(z, t-\tau) d\tau \,. \qquad (2\text{-}2)$$

Figure 2-2(c) illustrates the thermoacoustic pressure at the ultrasonic transducer generated from the slab, which was obtained by convolving the two temporal waveforms in Figs. 2-2(a) and 2-2(b) by use of Eq. (2-2).

The experimentally measured piezo-electric impulse response $q(t)$ of the ultrasonic transducer is shown in Fig. 2-2(d). The piezo-electric output of the ultrasonic transducer in response to thermoacoustic pressure can be calculated by the following convolution between the thermoacoustic pressure at the transducer and the impulse response of the transducer:

$$P_o(z,t) = \int p(z,\tau) q(\tau - t) d\tau \,. \qquad (2\text{-}3)$$

The piezo-electric signal from a 4.8-mm slab was obtained by the convolution of the two waveforms in Figs. 2-2(c) and (d) with Eq. (2-3) and is plotted in Fig. 2(e) as a dashed line.

The experimental piezo-electric signal from a 4.8-mm gel slab is plotted in Fig. 2-2(e) as a solid line for comparison, where the slight offset was caused by the DC drift of the amplifier in the experimental detection. There are two dipolar structures in each waveform in Fig. 2-2(e), and the signal between the dipolar structures is weak. The dipolar structures from the upper and lower surfaces of the slab have opposite polarities, which could not be explained by any existing theories in the literature. The polarity, the width of each dipole, and the distance between the two dipolar structures are in good agreement between the results of our theory and experiment. Because the piezo-electric signal of the ultrasonic transducer can be simulated by the two convolutions as shown above, the dipole width is related to the width of the microwave pulses and the width of the impulse response of the ultrasonic transducer, which were 0.5 μs and 1.7 μs, respectively. The time intervals between the zero-crossing points of the two dipolar structures in the two waveforms are determined by the slab thickness and are equal to the acoustic transit time 3.2 μs over the 4.8-mm-thick slab.

Dipolar structures were also observed in photoacoustics by lasers, where a Q-switched laser with a pulse width of ~10 ns and a wideband ultrasonic transducer were employed. Our detected dipolar structures resemble the well-known dipolar structures that originate from small spherical or cylindrical objects excited by laser pulses[61] or from acoustic reflection at soft acoustic interfaces.[62] However, our detected dipolar structures in the thermoacoustic signals in slabs resulted from the limited bandwidth of the ultrasonic transducers.

2. In frequency domain

This phenomenon can also be explained in the frequency domain, where the ultrasonic transducer acts as a band-pass filter. A frequency spectrum of the ultrasonic transducer is shown in Fig. 2-3(a). The temporal profile of the thermoacoustic pressure varies sharply near the slab boundaries and slowly inside the slab as shown in Fig. 2-2(c). The corresponding spectrum is peaked at DC as shown in Fig. 2-3(b). The filtered spectrum is peaked near 0.5 MHz as shown in Fig. 2-3(c), where the DC is rejected and the low-frequency components are attenuated significantly. In other words, the ultrasonic transducer cannot respond efficiently to the thermoacoustic waves emitted between the sample boundaries, which have a lower-frequency spectrum. Therefore, the observed piezo-electric signal between the two sample boundaries is low.

This model includes only the key concept. Scattering and diffraction of microwaves becomes certainly important if strictly quantitative modeling is performed. The detected thermoacoustic signals are also related to other factors including microwave attenuation, conversion efficiency from microwave energy to acoustic energy, acoustic scattering and diffraction, and acoustic attenuation.

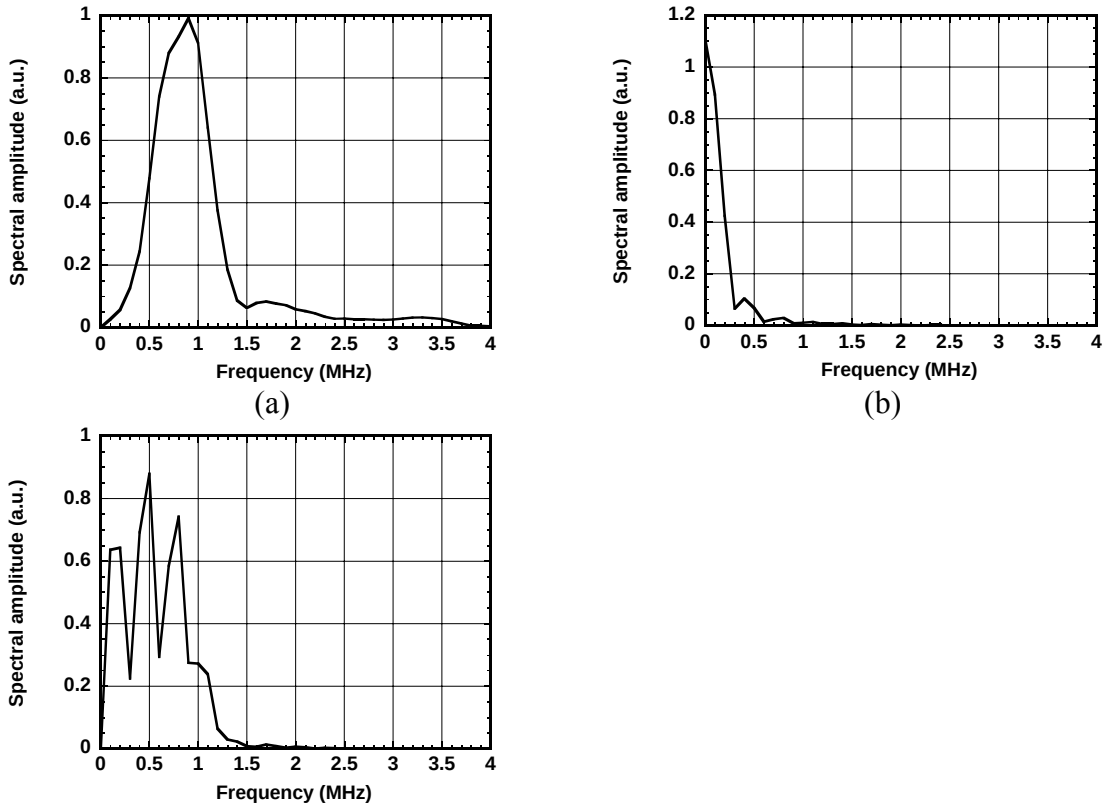

Figure 2-3. Frequency-domain analysis of the microwave-induced thermoacoustic signals. (a) Spectrum of the 1-MHz ultrasonic transducer; (b) Spectrum of the microwave-induced thermoacoustic signal; (c) Spectrum of the piezo-electric signal, which was the filtered microwave-induced thermoacoustic signal.

D. THERMOACOUSTIC IMAGE OF TISSUES' MICROWAVE CONTRAST

A tissue sample with a fat-muscle-fat structure as shown in Fig. 2-4(a) was placed on the plastic stand inside the container as shown in Fig. 2-1. Figure 2-4(b) shows a 2D image of the sample obtained with the scanning thermoacoustic tomography technique. Thermoacoustic signals were acquired in the time domain while the fat-

muscle-fat sample was scanned horizontally along the *y* axis with a step size of 1 mm. The 2D image of the sample was formed by combining these temporal waveforms taken successively at the scanning stops along the *y* axis. Each vertical line in this 2D image was from a temporal waveform. The muscle inside the fat is clearly visible with a good contrast. The fat-tissue interface to the left of the muscle is also visible, which was possibly caused by the slight difference in the microwave properties between the two fat sections.

Figure 2-4(c) illustrates a time-domain waveform that was measured above the center of the sample at *y* equal to 54 mm. The strongest dipole near 27 μs was from the bottom boundary of the sample where microwave experienced the least attenuation, whereas the weakest dipole near 14 μs was from the top boundary of the sample where microwave experienced the most attenuation. The two dipolar structures corresponding to the boundaries of the muscle layer are also clearly distinguishable. The time intervals between the adjacent dipolar structures agree with the thickness values of the tissue layers very well. However, the vertical boundaries of the muscle slab are not visible in the image because the thermoacoustic waves from these boundaries propagate perpendicularly to the acoustic axis of the ultrasonic transducer and therefore cannot be received by the transducer.

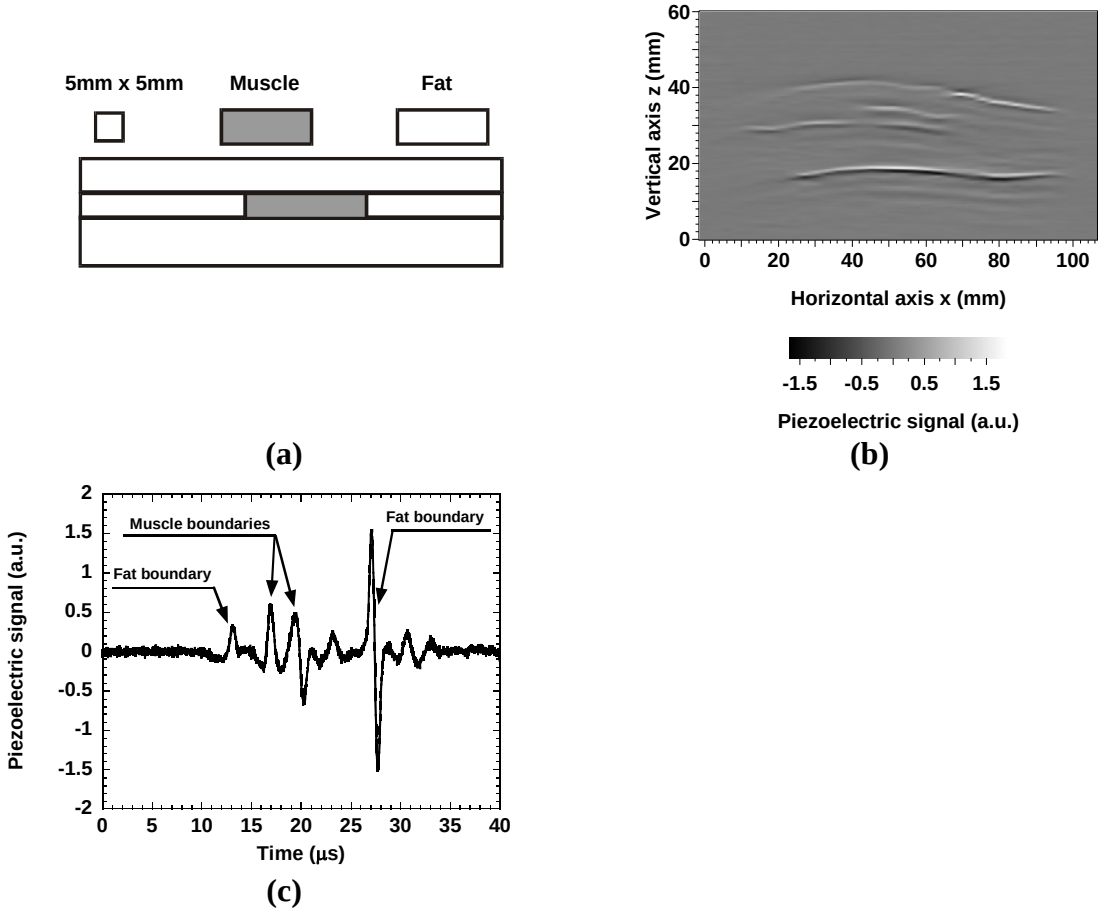

Figure 2-4. (a) Cross section of a fat-muscle-fat sample on the *y*-*z* plane; (b) Two-dimensional image of the *y*-*z* cross section of the sample obtained by scanning thermoacoustic tomography; (c) Temporal microwave-induced thermoacoustic signal along the vertical center line of the sample. The 1-MHz ultrasonic transducer was used in this experiment.

E. THERMOACOUSTIC IMAGING RESOLUTION

1. Axial resolution

The axial resolution along the acoustic axis (*z* axis) is determined by the width of the thermoacoustic dipolar structures, which is related to the width of the microwave pulse and the width of the impulse response of the transducer (the inverse of the bandwidth of the ultrasonic detector). When the 1-MHz ultrasonic transducer was used, the width of the thermoacoustic signal was estimated to be 2.2 μs, which was the sum of the width of the microwave pulses (0.5 μs) and the width of the impulse response of the transducer (1.7 μs). Because the speed of sound in tissue is ~1.5 mm/μs, the corresponding axial resolution should be approximately 3.3 mm along the *z* axis. For the 3.5-MHz ultrasonic transducer, the axial resolution should be improved to 1.4 mm theoretically.

Figure 2-5 shows the thermoacoustic signals from slab samples of various thickness values measured by the 1-MHz ultrasonic transducer. The slab samples were made of 5% gelatin and 5% NaCl, where NaCl controlled the microwave absorption. As the thickness of the samples decreased, the temporal distance between the adjacent dipolar structures corresponding to the two boundaries of the slabs decreased as well. The two dipolar structures became barely distinguishable when the thickness was reduced to 3.8 mm and completely inseparable when the thickness was reduced to 2 mm. Therefore, the experimentally measured axial resolution was ~3.8 mm, close to the above calculated resolution of 3.3 mm based on the dipole width. The discrepancy was

caused by the long tail of the dipolar structures. The relative variation in intensity between the two dipolar structures was caused by microwave attenuation in the slabs.

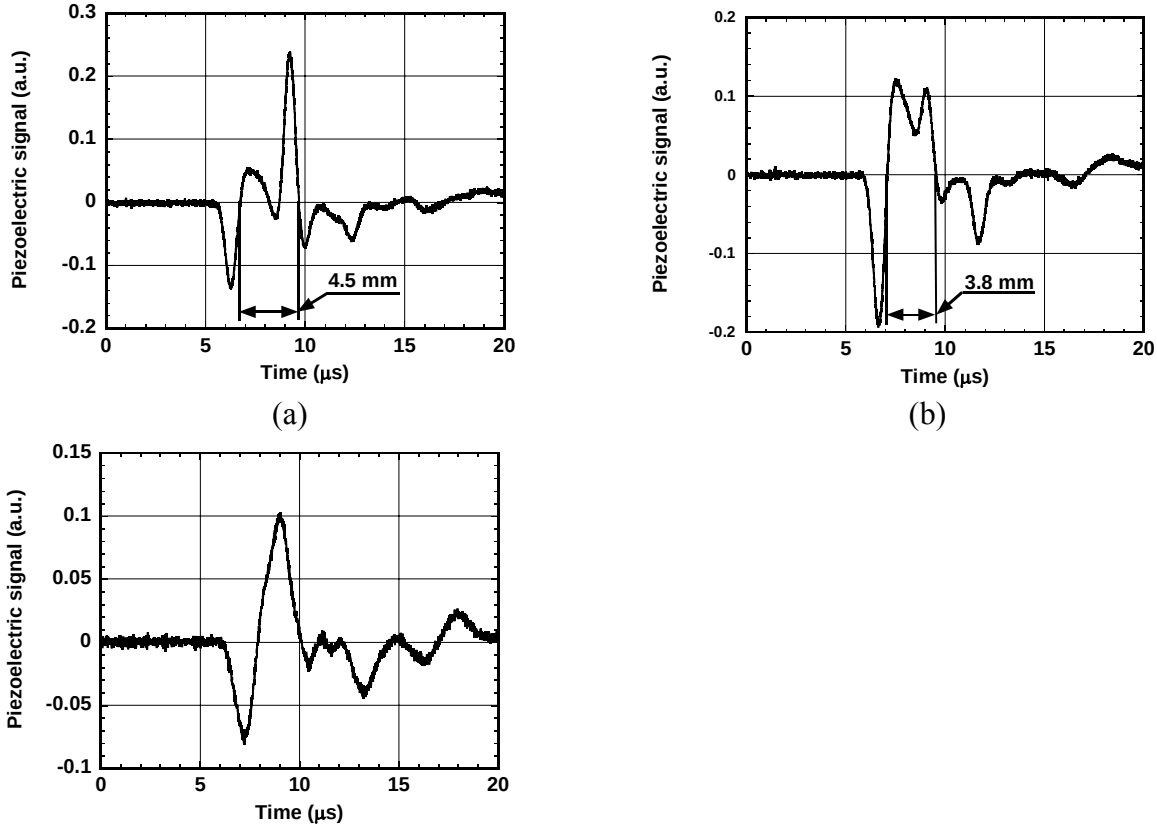

Figure 2-5. Microwave-induced thermoacoustic signals in gel slabs of various thickness values: (a) 4.5 mm, (b) 3.8 mm, and (c) 2 mm. The 1-MHz ultrasonic transducer was used.

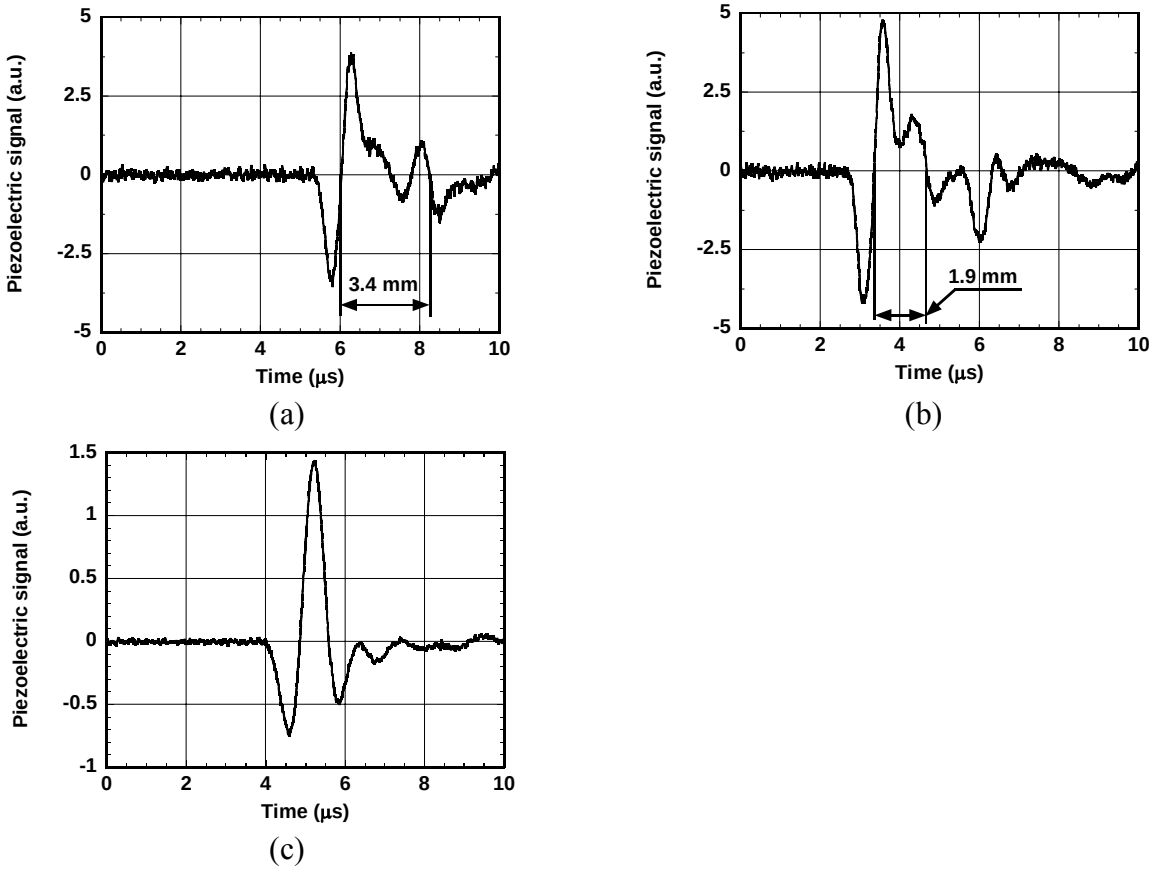

Figure 2-6. Microwave-induced thermoacoustic signals in gel slabs of various thickness values: (a) 3.4 mm, (b) 1.9 mm, and (c) 1 mm. The 3.5-MHz ultrasonic transducer was used.

Similarly, Figure 2-6 shows the thermoacoustic signals from slab samples of various thickness values measured by the 3.5-MHz ultrasonic transducer. The experimentally measured axial resolution was ~1.9 mm, close to the above calculated resolution of 1.4 mm based on the dipole width. As expected from the theoretical consideration, the wider-bandwidth transducer produced better axial resolution. Potentially, shorter microwave pulses and deconvolution may be used to improve the axial resolution further.

2. Lateral resolution

The lateral resolution is determined by the numerical aperture of the ultrasonic transducer. The ultrasonic transducer responds to the thermoacoustic signals along its acoustic axis. The detected source area is related to the numerical aperture of the ultrasonic transducer and the distance between the thermoacoustic source and the ultrasonic transducer. The minimum detected source area is at the focal plane of the ultrasonic transducer. Therefore, a better lateral resolution is expected when the sample is located within the focal column. We examined the lateral resolution with the 1-MHz ultrasonic transducer. The ultrasonic transducer has a 3-dB focal diameter of 2.1 mm and a focal zone of 17.6 mm along the acoustic axis. Several pieces of rectangular gel slabs were arranged linearly along the *y* direction as shown in Fig. 2-7(a). The *y*-*z* cross section was imaged with a step size of 1 mm when the sample was scanned along the *y* axis. Figure 2-7(b) shows the two-dimensional image when the sample was on the focal plane of the ultrasonic transducer. The bright upper band near $z = 14$ mm is the primary image from the thermoacoustic waves propagating directly upward toward the ultrasonic transducer, whereas the dark lower band near $z = 9$ mm is the "ghost" image caused by acoustic reflection from the plastic stand. The gaps of greater than 4 mm can be easily recognized. The gap of 2.5 mm can be barely identified, which defines the lateral resolution and is comparable with the focal diameter of the ultrasonic transducer.

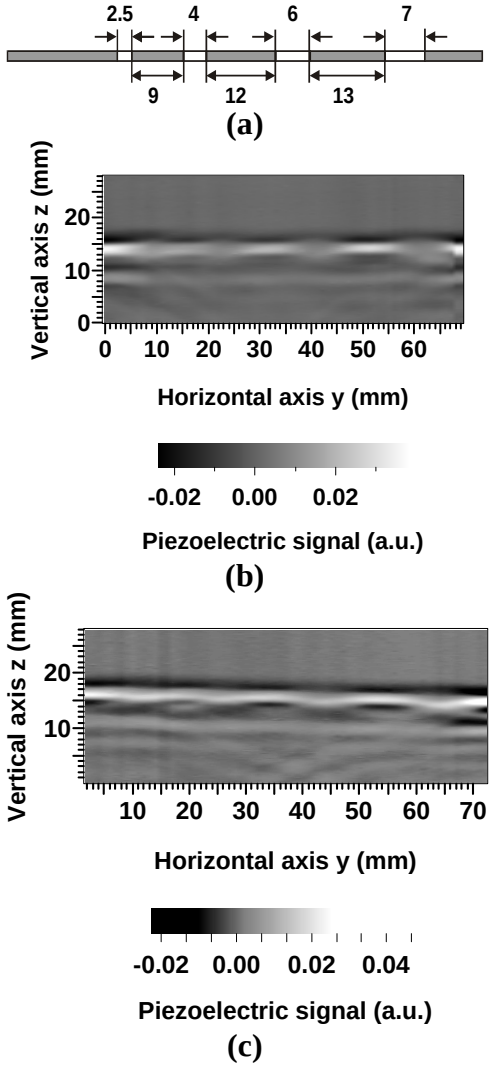

Figure 2-7. Two-dimensional tomographic images of a linear array of gel slabs obtained by scanning thermoacoustic tomography. (a) *y*-*z* cross section of the sample (units in mm); (b) Image of the *y*-*z* cross section when the sample was placed at the focal plane of the ultrasonic transducer; (c) Image of the *y*-*z* cross section when the sample was placed far from the focal plane of the ultrasonic transducer.

The measured thermoacoustic signal is a convolution between the thermoacoustic signal in the sample and the detection-sensitivity distribution of the ultrasonic transducer over the detected area. The convolution reduces the lateral resolution, which is worsened when the ultrasonic transducer is out of focus. Figure 2-7(c) was acquired when the ultrasonic transducer was deliberately moved far away from the sample so as to create defocusing. The gaps are not distinguishable in the 2D image due to reduced resolution.

CHAPTER III

SCANNING THERMOACOUSTIC TOMOGRAPHY

A. THERMOACOUSTIC IMAGING OF BIOLOGICAL TISSUES

We further investigated scanning microwave-induced thermoacoustic tomography toward biomedical applications. The piezoelectric signal, which is related to the thermoacoustic contrast, was simulated over a wide range of electromagnetic frequency and depth of tumor location based on the microwave-absorption properties of normal and cancerous breast tissues. The imaging resolutions were investigated in relation to the experimental parameters. Images of thick biological tissue samples were acquired experimentally, which clearly revealed the artificially buried tissue objects and the intrinsic structures as well. Gain compensation based on electromagnetic attenuation was applied to enhance the image contrast.

B. EXPERIMENTAL SETUP

The experimental setup for this study is shown in Fig. 3-1. A Cartesian coordinate system was set up for reference. The *z* axis was along the acoustic axis pointing upward. The *x* axis was perpendicular to the drawing plane and pointed outward. The *y* axis was in the drawing plane pointing to the right.

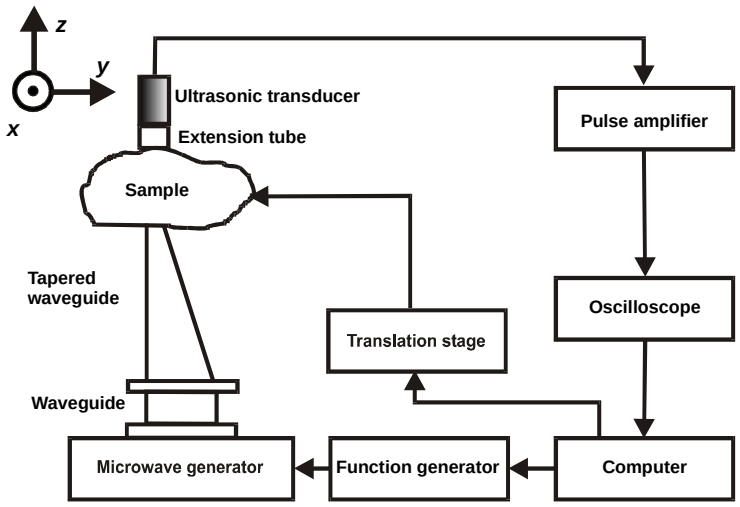

Figure 3-1. Experimental setup for scanning thermoacoustic tomography.

A 3-GHz microwave generator transmitted microwave pulses toward the tissue samples. The pulse width was set to 0.5 μs for most of the experiments unless it is stated otherwise. The energy of a single microwave pulse was estimated to be 5 mJ. A function generator (DS345, Stanford Research System) was employed to trigger the microwave generator, control its pulse repetition frequency, and synchronize the oscilloscope sampling. Microwave energy was delivered through two waveguides in tandem: a standard rectangular waveguide with a cross section of 72 mm × 34 mm and a tapered waveguide that narrowed the output cross section to 72 mm × 5 mm. The narrow output port helped concentrate the microwave energy into the imaging zone in the samples. Using tapered waveguide increases the input microwave energy intensity, but input beam shape becomes more like a line source from a plane source, and then its power attenuates in tissue along the propagation direction proportional to the square root of the imaging depth. Therefore, we should trade off the power density and its

attenuation according to the size of imaged object. In our experiment, the object to be imaged was placed on a plastic holder. The holder was fixed onto a two-dimensional *x*-*y* translation stage (MD2, Arrick Robotics). A personal computer controlled the two stepper motors to drive the translation stage in the *x* and *y* directions. An extension tube filled with acoustic-coupling water was mounted onto the ultrasonic transducer. The length of the extension tube was determined such that its focal zone was inside the region of imaging interest in the samples. The bottom surface of the extension tube was in contact with the samples for good acoustic coupling. The central frequency of the ultrasonic transducer (V314, Panametrics) was 1 MHz, the bandwidth was 0.6 MHz, the diameter was 1.9 cm, the focal length was 2.5 cm, and the focal diameter at 1 MHz was 0.2 cm. The piezoelectric output of the ultrasonic transducer was connected to a pulse amplifier (500PR, Panametrics). The amplified signal was averaged 10-100 times by an oscilloscope (TDS-640A, Tektronix) and then transferred to the personal computer.

C. MICROWAVE ATTENUATION AND ABSORPTION IN TISSUES

Because the propagation speed of electromagnetic waves is much greater than the speed of sound, the microwave pulses stimulated the entire tissue sample essentially simultaneously. The induced thermoacoustic waves took different amounts of time to reach the ultrasonic transducer. The ultrasonic transducer measured the time of arrival of the thermoacoustic waves. The distance between the acoustic sources and the transducer was calculated by multiplying the time of arrival with the speed of sound in the medium. Because the ultrasonic transducer was focused, it responded primarily to the acoustic sources along its focal column. Therefore, a time-domain signal was

converted into a one-dimensional image along the transducer axis (z axis), which is similar to an ultrasonic A-scan. Scanning the sample along the x or y axis yielded a two-dimensional cross-sectional image of the sample.

1. Stimulation power attenuation

The narrow elongated output port of the tapered waveguide may be considered as a "line source" of electromagnetic radiation. Cylindrical wave propagation was assumed throughout the frequency range in our simulation of the thermoacoustic signal, although waveguides are rarely employed in practice for the low-frequency region of the considered electromagnetic spectrum. An electromagnetic wave was emitted from the tapered waveguide and attenuated in tissue approximately as

$$I(z) = I_0 \frac{\exp(-2\alpha z)}{\sqrt{z}}, \qquad (3\text{-}1)$$

where I_0 is the intensity at the output port of the tapered waveguide, z is the distance from the output port to the point of observation along the vertical axis, $I(z)$ is the intensity at z, and α is the field absorption coefficient in tissue.

The absorption coefficient can be expressed as

$$\alpha = \omega \sqrt{\frac{\mu\varepsilon}{2}\left[\sqrt{1+\left(\frac{\sigma}{\omega\varepsilon}\right)^2}-1\right]}, \qquad (3\text{-}2)$$

where ω is the angular frequency, μ is the permeability, ε is the permittivity, and σ is the conductivity. In the frequency range of 0.1-10 GHz, the dielectric constant (ratio of the permittivity in the material to that in vacuum) has a value of 5-70 for soft

tissues, and the conductivity has a value of 0.02-3 Ω^{-1} m^{-1}.[63-65] The complex dielectric properties of tissues at various microwave frequencies determine the propagation and absorption distribution of microwave. Consequently, the induced thermoacoustic pressure depends on the intensity of microwave and the complex dielectric constant of the material.

2. Thermoacoustic signal and imaging contrast

A simplified model was used to estimate the microwave-induced thermoacoustic pressure. A small breast tumor was embedded in normal breast tissue. The normal tissue predominantly determined the microwave attenuation. The thermoacoustic pressure p is proportional to the local absorbed microwave power:

$$p \propto I_0 \frac{2\alpha \exp(-2\alpha z)}{\sqrt{z}}. \qquad (3\text{-}3)$$

The ultrasonic transducer responds to the thermoacoustic components within its response bandwidth and rejects the components outside the bandwidth. The piezoelectric signal V_p from the ultrasonic transducer is proportional to the thermoacoustic contrast:

$$V_p \propto (p_t - p_n), \qquad (3\text{-}4)$$

where p_t and p_n are respectively the thermoacoustic pressures in the tumor and the normal background tissue at depth z where the tumor and the normal tissue interface. Based on Eqs. (3-3) and (3-4), we obtain

$$V_p \propto I_0 \frac{2(\alpha_t - \alpha_n)\exp(-2\alpha_n z)}{\sqrt{z}}, \qquad (3\text{-}5)$$

where α_t and α_n represent the microwave-absorption coefficients of the tumor and the normal breast tissue, respectively.

Figure 3-2(a) shows the penetration depth of electromagnetic waves in various human tissues as a function of the electromagnetic frequency in the radio frequency (RF) region, where the penetration depth is the inverse of the absorption coefficient.

The penetration depths of muscle and fat tissues are plotted in solid lines.[66] At the frequency of our experimental setup, 3 GHz, the penetration depths for fat and muscle are 9 cm and 1.2 cm, respectively. The penetration depths of normal and malignant human breast tissues are plotted in dashed lines.[67] At 3 GHz, the penetration depths for malignant and normal breast tissue are approximately 2.3 cm and 4.4 cm, respectively.

Water and ion concentrations are key factors in microwave absorption.[68] Muscle and fat tissues respectively have very high and very low water contents and therefore have the extreme microwave absorption properties. Most other soft tissues have an absorption coefficient in between those for muscle and fat tissues. This wide range of values among various tissues is desired for a high imaging contrast. Malignant breast tissues are more strongly absorbing than surrounding normal breast tissues.[69,70]

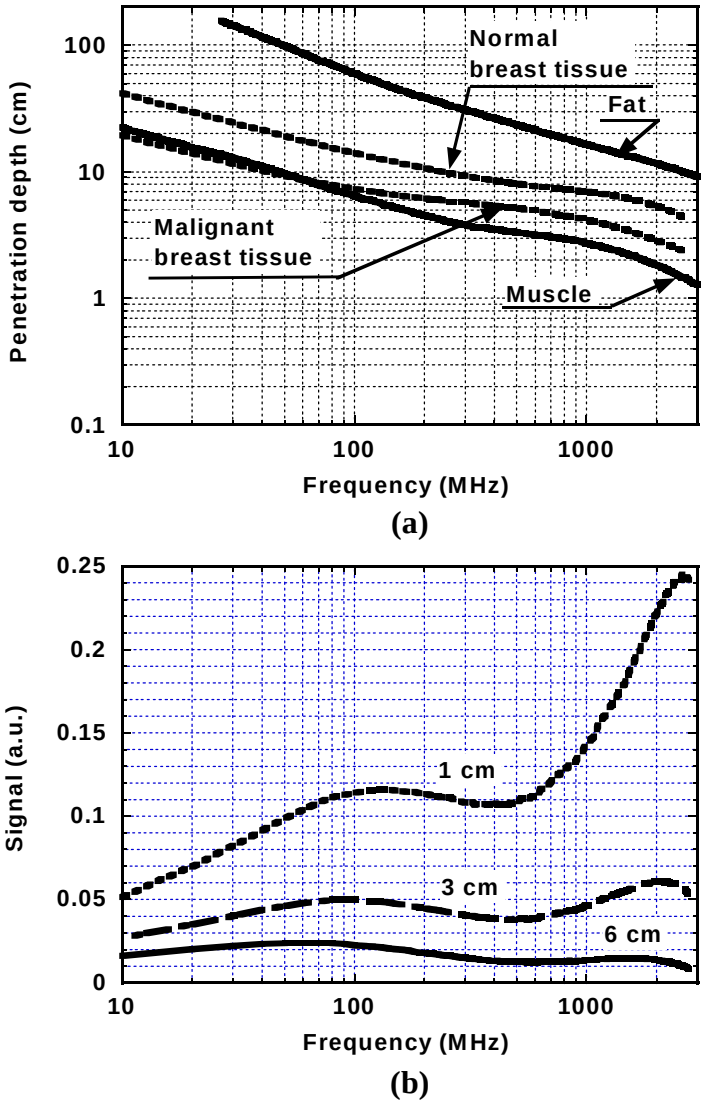

Figure 3-2. (a) Penetration depths of various biological tissues versus microwave frequency; (b) Simulated piezoelectric signal in response to a thermoacoustic wave from tissue containing a buried tumor versus microwave frequency.

We calculated the piezoelectric signal as a function of the electromagnetic frequency and tumor location using Eq. (3-5) [Fig. 3-2(b)]. If the detection system is instrument-noise limited, the signal-to-noise ratio (SNR) of the system is different from

this piezoelectric signal by a constant factor. The noise in our detection system was mainly from the pulse amplifier, which was used to amplify the piezoelectric signal from the ultrasonic transducer. The noise remained almost constant in our experiment and was independent of the microwave frequency or the depth of the tumor. The SNR decreases as the tumor location increases because of the increasingly attenuated microwave intensity. When the tumor is located near the tissue surface, e.g., at 1 cm depth, the SNR is better at higher frequencies. When the tumor is located more deeply, the choice of frequency for an optimal SNR is rather broad. This is because the decrease in thermoacoustic pressure is compensated by the increasing difference of the RF-absorption coefficients between the tumor and normal breast tissues as the frequency increases.

D. SCANNING THERMOACOUSTIC IMAGING

1. Signal convolution and axial resolution

The axial resolution is limited by two factors: the temporal width of the microwave pulse and the temporal width of the impulse response of the ultrasonic transducer. The temporal width of the impulse response of the ultrasonic transducer is inversely proportional to the bandwidth of the ultrasonic transducer. To illustrate the effect of the microwave-pulse width on the axial resolution, we simulated the thermoacoustic pressures and the corresponding piezoelectric signals from a microwave-absorbing slab of 5 mm in thickness using Eq. (3-3) and the convolution method

described previously. The excitation microwave pulses had the same peak power but different pulse widths: 1.0 μs, 0.5 μs, and 0.1 μs [Fig. 3-3].

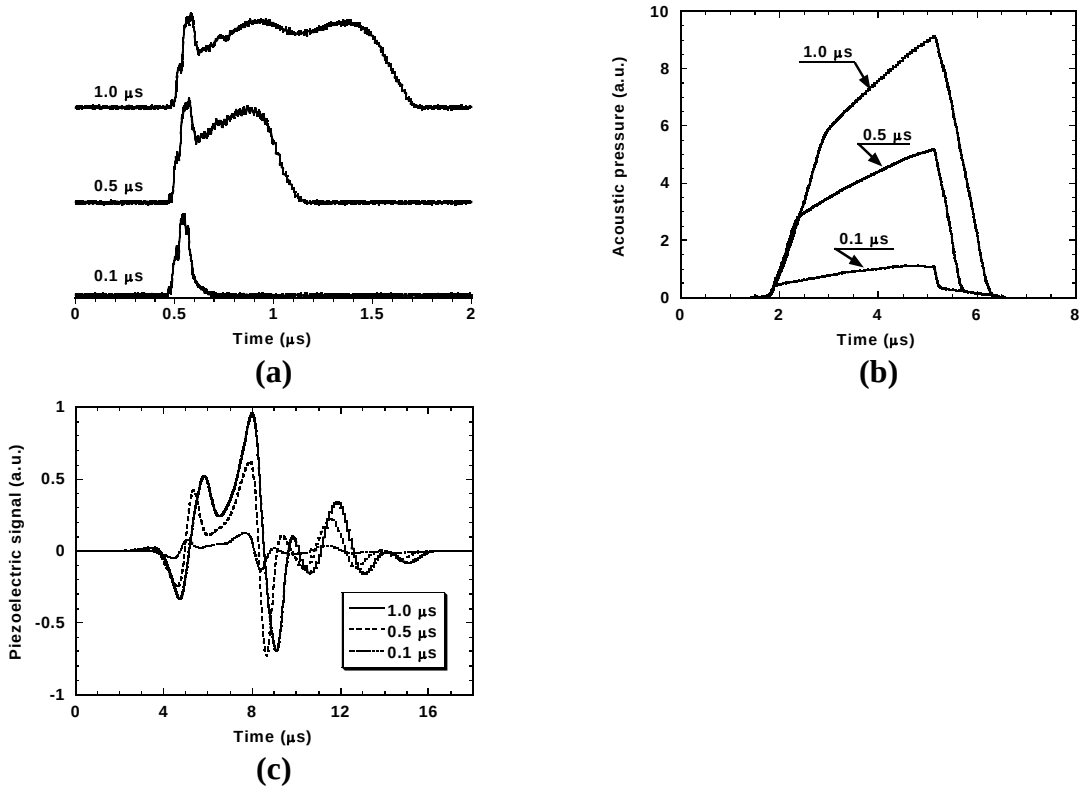

Figure 3-3. (a) Waveforms of the microwave pulses of various pulse widths tested in the experiment; (b) Simulated thermoacoustic waves from a 5-mm-thick microwave-absorbing slab by the microwave pulses; (c) Simulated piezoelectric signals of the thermoacoustic waves in Fig. 3-3(b).

There are two dipolar structures corresponding to the two boundaries of the slab. The width of the dipolar structures is determined by the width of the microwave pulses and the impulse response time of the ultrasonic transducer. The distance between the

dipolar structures is determined by the acoustic-transit time across the slab. For the 5-mm thick slab, the acoustic-transit time was 3.3 μs based on the speed of sound of ~1.5 mm/μs. Pumping with a narrower microwave pulse decreases the width of the dipolar structures and therefore improves the axial resolution because the dipolar structures define the time window for the axial resolution. The narrower microwave pulses of the same peak pressure also produce smaller signals. Likewise, an ultrasonic transducer of a higher central frequency and a broader bandwidth produces narrower dipolar structures and therefore improves the axial resolution at the expense of signal strength.

2. Numerical aperture and lateral resolution

The lateral resolution at the focal plane is limited by the focal diameter of the ultrasonic transducer. Based on the ultrasound reciprocity, the focal diameter determines both the beam diameter when the ultrasonic transducer transmits ultrasound and the detection directivity factor when the ultrasonic transducer detects ultrasound. The focal diameter is approximately determined by

$$\phi_f = \lambda_a / \mathrm{NA} = c_a /(\mathrm{NA} f_a), \qquad (3\text{-}6)$$

where λ_a represents the acoustic wavelength, NA represents the numerical aperture of the ultrasonic transducer, c_a represents the speed of sound, and f_a represents the central frequency of the piezoelectric signal. The numerical aperture NA is solely determined by the ultrasonic transducer. The speed of sound c_a is relatively constant throughout the frequency range. The central frequency of the piezoelectric signal f_a is determined by the frequency spectrum of the thermoacoustic signal in the dipolar

structures and the frequency response of the ultrasonic transducer. Therefore, the lateral resolution is not only related to the ultrasonic parameters including the numerical aperture and the frequency response of the ultrasonic transducer but also related to the frequency content of the thermoacoustic signal in the dipolar structures. A high frequency is obviously desired for high-resolution imaging.

3. Detection bandwidth and imaging resolution

The ultrasonic transducer functions as a frequency filter to the thermoacoustic signals. The homogeneous tissue between interfaces produces slowly varying pressure signals caused by electromagnetic propagation and absorption. The slowly varying signals are outside the bandwidth of the ultrasonic transducer and therefore rejected. The variations in microwave absorption at tissue interfaces cause abrupt changes in thermoacoustic pressure. The abruptly varying signals have frequency components falling into the response bandwidth of the ultrasonic transducer and provide main contribution to the piezoelectric signals of the ultrasonic transducer. An ultrasonic transducer of a higher central frequency would provide better lateral resolution. An ultrasonic transducer of a higher central frequency usually has a broader bandwidth and would consequently yield better axial resolution as well. When the resolution is improved by varying the ultrasonic parameters, the SNR is reduced because the volume of thermoacoustic signal contributing to the piezoelectric signal is reduced. Therefore, there is a trade-off between imaging resolution and SNR.

It is worth noting that biological tissue itself also functions as a frequency filter to the thermoacoustic signals. Higher-frequency components experience greater

attenuation than the lower-frequency components. This attenuation is severe for the high-frequency components that pass through a long path in biological tissue. The preferential reduction in the high-frequency components would adversely affect the imaging resolution.

E. SCANNING THERMOACOUSTIC IMAGES OF BIOMEDICAL TISSUES

Two samples were prepared for our microwave-induced thermoacoustic imaging system to image. The background of the first sample was made intentionally as homogeneous as possible. A piece of muscle tissue was embedded into lard before it solidified, where the lard was used for its homogeneity. The sample was cut across to reveal the cross section after it was imaged with scanning thermoacoustic tomography after imaging experiment [Fig. 3-4]. The time-resolved thermoacoustic signals were acquired at each step while the sample was scanned horizontally along the y axis with a step size of 1 mm. Each vertical line in this two-dimensional thermoacoustic image was obtained from a temporal thermoacoustic waveform. Figure 3-4(c) shows the temporal thermoacoustic signal for y equal to 23 mm as an example. The earliest arriving signal came from the upper surface of the lard. The following signals corresponded to the two surfaces of the muscle and the bottom surface of the lard.

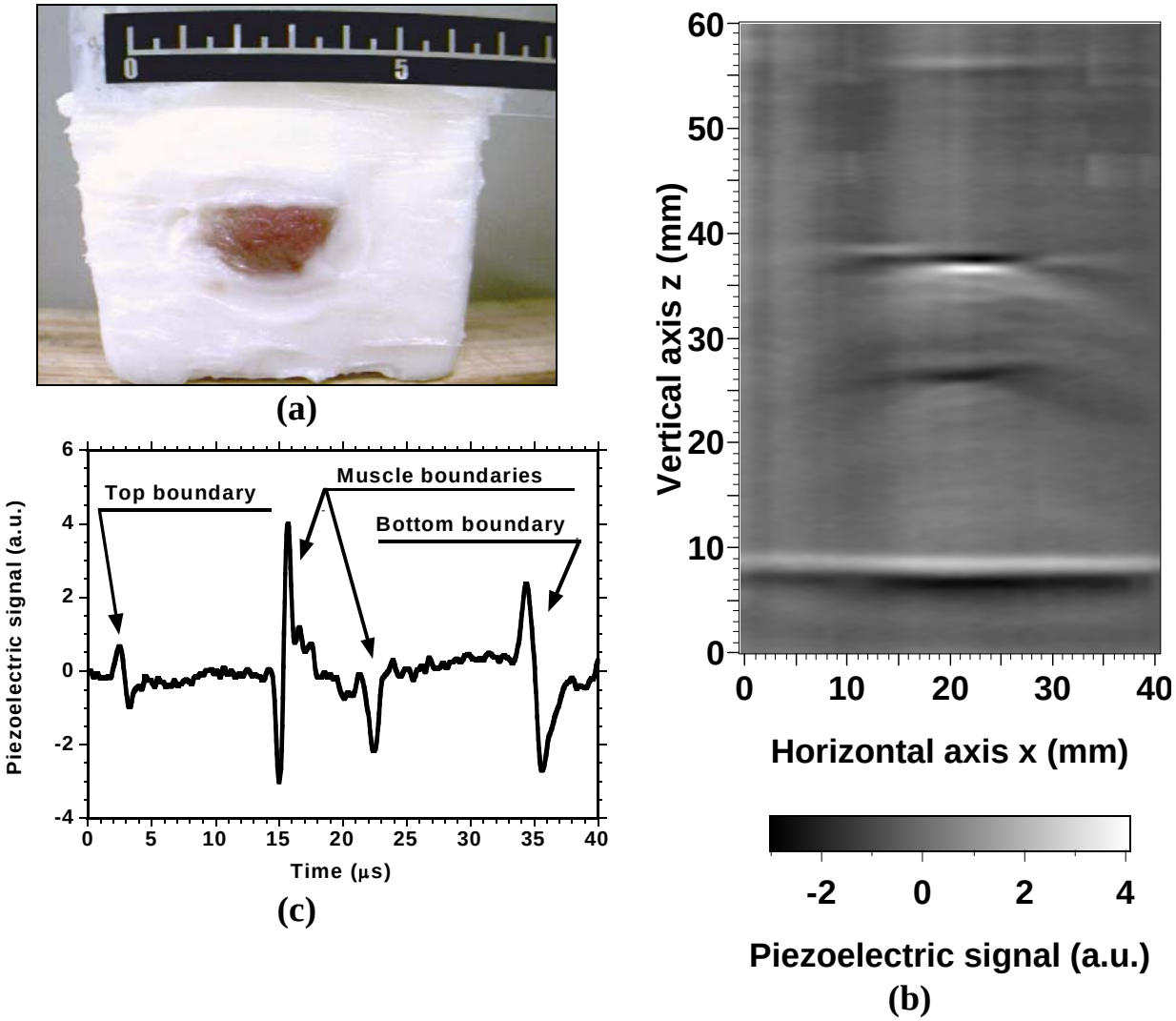

Figure 3-4. (a) Photograph of a *y*-*z* cross section of a lard sample containing a piece of muscle tissue, which was taken after the sample was imaged with the scanning thermoacoustic imaging system; (b) Two-dimensional thermoacoustic image of the cross section; (c) Typical temporal thermoacoustic signal corresponding to a vertical line in the two-dimensional thermoacoustic image.

Because the sample is in the near field of microwave, a logical question is whether the heterogeneity of the electromagnetic field would cause heterogeneity in thermoacoustic images. As shown in Fig. 3-4, the signal from the background lard is very weak, indicating the heterogeneity of the electromagnetic field does not affect thermoacoustic imaging significantly. The heterogeneity of the electromagnetic field is of the scale of the wavelength. The wavelength is several centimeters in biological tissue at the 3-GHz frequency. Spatial variations of this scale correspond to low-frequency thermoacoustic signals and are therefore filtered out by the ultrasonic transducer.

The background of the second sample was left with some heterogeneity. A piece of swine muscle tissue of ~5 mm in thickness was buried inside a piece of swine fat tissue. The fat tissue was naturally separated into several layers by thin (<1 mm in thickness) connective tissue that has greater microwave absorption than the adjacent fat tissue. A cross section of the sample was exposed and photographed after the sample was imaged with our scanning thermoacoustic imaging setup [Fig. 3-5]. Both the buried muscle and the connective tissue are clearly visible.

Because of microwave attenuation in tissue, the deeper tissue structures received less microwave radiation and produced weaker thermoacoustic signals. Consequently, the deeper structures were not as clearly imaged as the shallower ones. To enhance the image contrast, we compensated the piezoelectric signal with the following factor:

$$g(z) = \sqrt{z}\,\exp(2\alpha z)\,, \qquad (3\text{-}7)$$

which is the inverse of microwave intensity attenuation. In Fig. 3-5(c), the original piezoelectric signal for y equal to 20 mm was plotted with a solid line. The microwave-induced thermoacoustic signal decreased for increasing distance z. The inverse of the compensated gain was added into the figure with a dashed line for a comparison with the decay of the original piezoelectric signal. The deeper signal would be compensated with a greater gain. The compensated data, plotted with a point-dashed line, had nearly constant amplitude throughout the imaged depth. The gain-compensated image [Fig. 3-5(d)] shows the deeper structures clearly as well. Some interference from the pulse amplifier was also amplified by the "gain compensation" and shown as the artifacts in the image near the upper surface of the muscle tissue. This technique is similar to the "time-gain compensation" in the conventional ultrasonography.

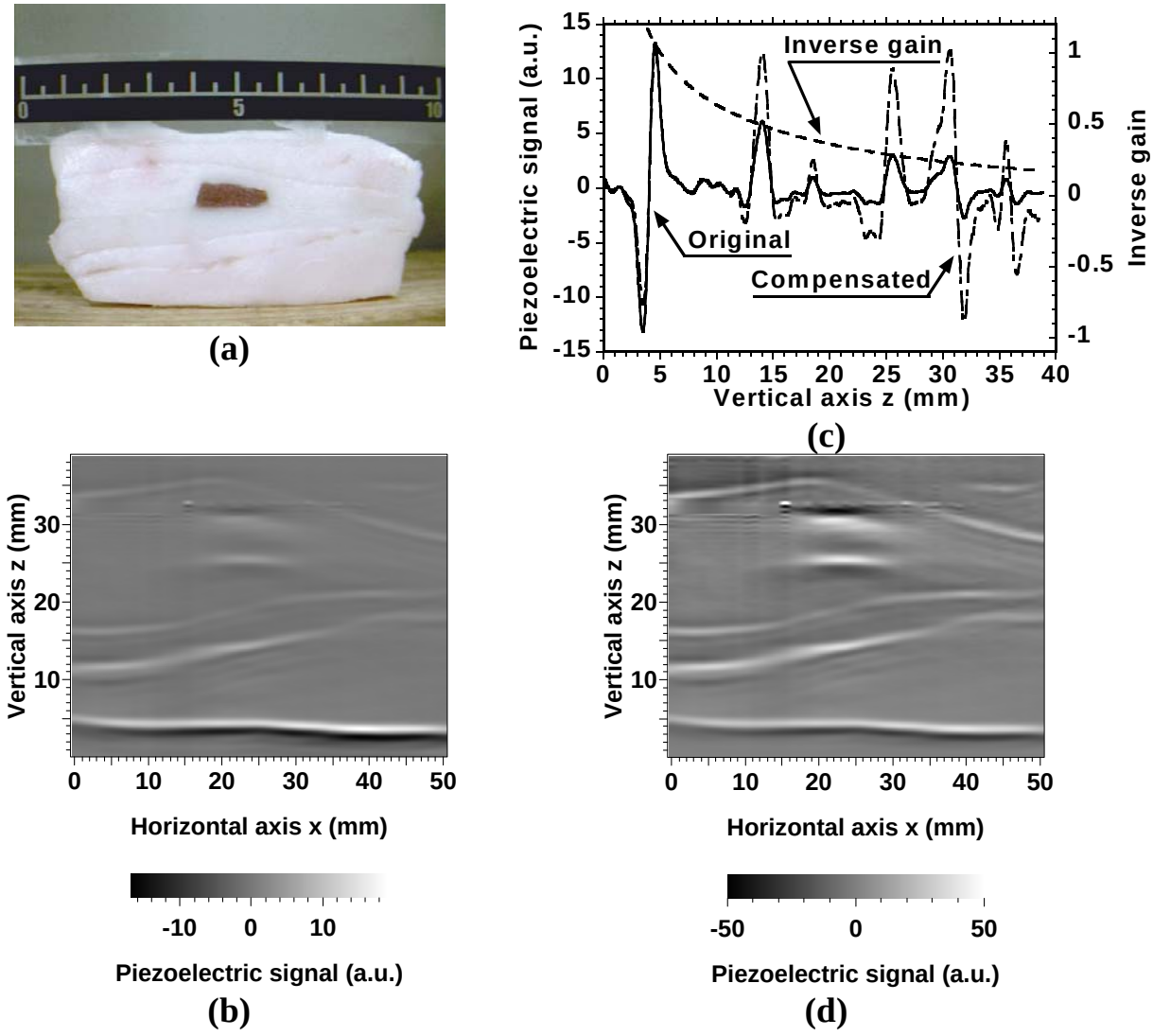

Figure. 3-5 (a) Photograph of a *y-z* cross section of a fat-tissue sample containing a piece of muscle tissue, which was taken after the sample was imaged with the scanning thermoacoustic imaging system; (b) Two-dimensional thermoacoustic image of the cross section; (c) Gain compensation to a typical piezoelectric signal; (d) Two-dimensional thermoacoustic image of the cross section after gain compensation.

CHAPTER IV

MULTIPLE-BANDWIDTH PHOTOACOUSTIC TOMOGRAPHY

A. PHOTOACOUSTIC SIGNALS AND THEIR DETECTION

Photoacoustic tomography is a nonionizing imaging modality for visualizing biological tissues with optical contrast and ultrasonic resolution. The induced acoustic signals from biological tissues exhibit the heterogeneity of optical absorption in the samples and reveal the structure of tissues. For some specified wavelength of light, the absorption coefficient of blood can be 10 times higher than that of its surrounding tissues.[23] Because fast developing tumors consume more blood, most malignant tumors have higher optical absorption. For example, the absorption contrast between breast tumors and normal breast tissues can be as high as 300% at the 1064-nm wavelength.[71] Another example is represented by the tumors of the nervous system, which in general are well vascularized, especially the most malignant ones such as glioblastoma multiforme (GBM). GBM is characterized by an increased vascular proliferation, cellular heterogeneity and necrosis. These characteristics reflect rich and distorted vasculature within the tumor. Intra-tumoral arteriovenous shunting and early filling of draining cerebral veins are commonly seen due to tumor-related neovascularization.[72] The laser-induced thermal expansion of an absorptive structure in tissues creates acoustic waves by the thermoelastic mechanism. The induced acoustic waves spread out through the medium and can be detected by ultrasonic detectors. Photoacoustic imaging

is based on ultrasonic propagation and detection, which means that it has the same good spatial resolution as pure ultrasound imaging.

The geometry of the region over which the ultrasonic transducer is scanned determines the imaging mode and the reconstruction algorithms. For the detection of layered structures of tissues or tumors under human epidermis, the ultrasonic transducer has to be placed on the skin along the laser beam to accomplish detection *in vivo*. Karabutov and Oraevsky *et al.*[73,74] presented photacoustic imaging with axial resolution up to 15 μm. The imaging of small deeply embedded tumors, such as breast tumors, was also studied by Esenaliev *et al.*[75] and Oraevsky *et al.* [71,76] Hoelen *et al*. employed a transducer array on a plane to detect induced signals from vascular systems.[77] The image was reconstructed using a delay-and-sum algorithm, where the depth resolution was better than 20 μm, and the lateral resolution was better than 200 μm. The detector can also scan over a circle.[78] Some reconstruction algorithms have been developed to use the signals from the scan to form an image. Examples of current reconstruction algorithms include the weighted delay-and-sum method,[7] the optimal statistical approach,[79] and the Radon transform in the far-field approximation.[21,80] Only recently have exact reconstructions been studied theoretically and reconstruction algorithms for various regular geometries derived.[81–84]

B. PHOTOACOUSTIC SIGNALS AND IMAGE RECONSTRUCTION

The generation, propagation, and detection of induced acoustic signals can be described by thermal expansion, wave equations and bandwidth filtering, respectively.[22] By directing the laser pulse on a test sample, the absorbed optical energy in tissue is

transformed into thermal energy, which is then, due to thermo-elastic expansion, converted into mechanical stress. If the energy deposition occurs rapidly in a time period that is much less than the thermal relaxation time and the stress relaxation time, the local pressure rise after heating can be derived as $\Delta p = \frac{\beta c^2}{C_p} E_a$, where Δp is the pressure rise; β is the isobaric volume expansion coefficient; c is the speed of sound; C_p is the specific heat; and E_a is the absorbed optical energy density.

The behavior of photoacoustic waves has been studied by Diebold and Gusev *et al*. based on the following non-homogenous wave equation:[85,86]

$$\nabla^2 p(\mathbf{r},t) - \frac{1}{c^2}\frac{\partial^2 p(\mathbf{r},t)}{\partial t^2} = -\frac{\beta}{C_p}\frac{\partial H(\mathbf{r},t)}{\partial t}, \qquad (4\text{-}1)$$

where $p(\mathbf{r},t)$ is the acoustic pressure at time t and position $\mathbf{r}$ and $H(\mathbf{r},t)$ is the heat function of the optical energy deposited in the tissues per unit volume per unit time, which can be expressed as

$$H(\mathbf{r},t) = A(\mathbf{r})I(t), \qquad (4\text{-}2)$$

where $A(\mathbf{r})$ describes the optical energy deposition within the tissues at position $\mathbf{r}$ (structure of tissues); and $I(t)$ describes the shape of the irradiation pulse, which can be further expressed as $I(t) = \delta(t)$ for impulse heating.

The purpose of photoacoustic tomography is to reconstruct the distribution of the optical absorption $A(\mathbf{r})$ in the tissues from a set of measured acoustic signals $p(\mathbf{r},t)$. For a cylindrical scanning configuration, the exact inverse solution can be derived. In

most practical image reconstruction, the algorithm can be simplified to shorten the reconstruction time. If the detection radius r_0 is much longer than the wavelength that corresponds to the central frequency of the detection device (far-field detection), we can assume $|k|r_0 >> 1$ and simplify the exact inverse solution to the form of[87]

$$A(\mathbf{r}) = -\frac{\beta}{2\pi c^4 C_p}\iint_{S_0} dS_0(\cos\Theta)\frac{1}{t}\frac{\partial p(\mathbf{r}_0,t)}{\partial t}\bigg|_{t=|\mathbf{r}_0-\mathbf{r}|/c} \qquad (4\text{-}3)$$

where S_0 is the surface over which the detectors are scanned; Θ is the angle between the normal line of the detector and the vector from the detector to the reconstruction point.

Induced acoustic waves range widely in the frequency spectrum. However, a single ultrasonic transducer can only respond to part of the spectrum because of its limited bandwidth.[88] In general, a transducer with a higher central frequency detects acoustic signals with a wider bandwidth, but the signal is weaker. Sometimes choosing the ultrasonic detector is a dilemma since a trade-off between imaging resolution (bandwidth) and sensitivity may be necessary. In this paper, we demonstrate a photoacoustic imaging experiment that simultaneously uses three transducers with the 3.5-MHz, 10-MHz and 20-MHz central frequencies, respectively. Images associated with the three transducers will be compared and analyzed. Further discussions on image resolution and signal-noise ratio (SNR) will be presented as well.

C. EXPERIMENTAL SETUP

The experimental setup for the photoacoustic tomographic system employing multiple ultrasonic transducers is shown in Fig. 4-1. A Q-switched pulsed Nd:YAG laser (Brilliant B, BigSky), operating at the second harmonic wave with a wavelength of 532 nm, is used as the pumping source. The laser pulse width is 6.5 ns and the pulse repetition rate is 10 Hz. The laser beam is expanded by a concave lens and homogenized by a ground glass and then is delivered to the test sample. The pulse energy density is controlled below ~20 mJ/cm^2, which is the maximum permissible exposure (MPE) for skin to a laser beam at a wavelength of 532 nm.[89]

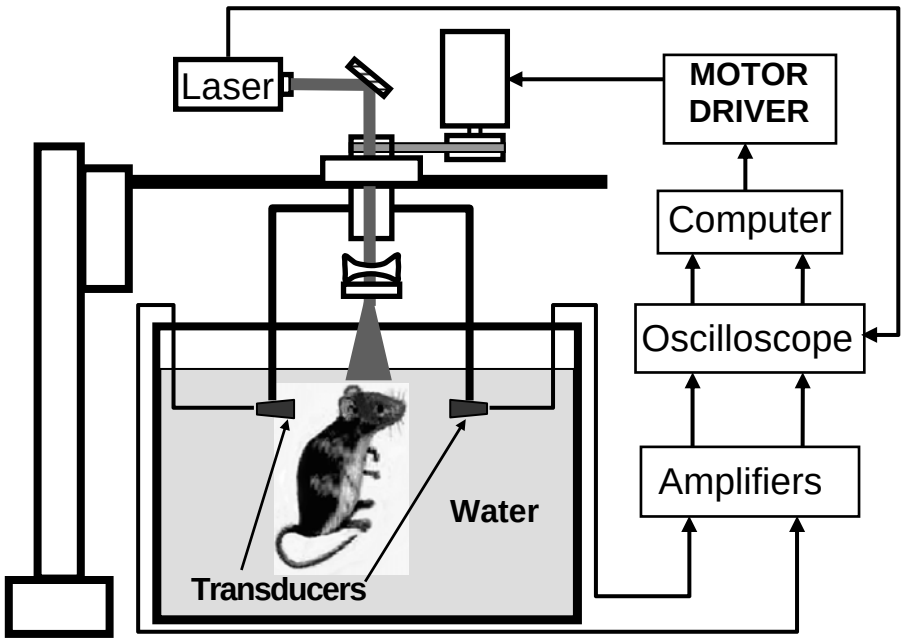

Figure 4-1. Experimental setup of photoacoustic tomography employing multiple ultrasonic transducers, each at a different frequency.

Three ultrasonic transducers (V383/3.5MHz, XMS-310/10 MHz, and V316-N/20MHz, Panametrics) are used as the detectors to receive the induced acoustic signals. The diameters of the active areas are 10 mm for the 3.5 MHz transducer, 2 mm for the 10 MHz transducer and 3 mm for the 20 MHz transducer, respectively. These commercial transducers have nominal bandwidths of 50% to 80% of their central frequencies.

A two-dimensional translation of the detectors is designed; one involves circular scanning in the horizontal plane, and the other involves linear scanning along the vertical direction. A rotational apparatus supported by two bearings is driven by a step motor to implement the circular scanning. The entire horizontal scanning section is made as one piece and then connected to an uprightly placed translation stage. Hence, the section of the circular scan can be impelled vertically. The transducers are attached to the rotational apparatus to complete circular scanning around the test sample. By combining the two movements, the transducers can scan in a cylindrical contour around the test sample.[90] However, we will report here only results based on one-dimensional circular scans. Typical scanning parameters in our experiment are 240 steps for a full view of 2π circular scanning (1.5°/step) and 10 steps in 12.7 mm range (1.27 mm/step) for vertical scanning.

The transducers convert the acoustic energy into electrical signals that are amplified by amplifiers (ZFL-500LN, Mini-Circuits). An oscilloscope with four channels (TDS-540A, Tektronix) is employed to monitor and record the acoustic signals. A LabView program controls the scanning of the transducers and the data acquisition

according to the following sequence: first, start the step motor to move the transducers to the arranged position; secondly, fire the laser and trigger the data acquisition; third, average the time-dependant signals on the oscilloscope to improve the SNR; finally, save the time-dependent data at this scanning stop. After that, the transducers are moved to the next scanning stop and the above procedure is repeated.

For coupling the induced acoustic signals, the transducers and the test sample are immersed in water in a container. The laser light is directed onto the test sample through a hole on the rotational axis. The head of an adult BALB/c mouse (Charles River Breeding Laboratories, ~27 g) was imaged using the above mentioned three transducers simultaneously. The hair on the mouse head was removed gently using hair remover lotion to improve light penetration.

D. IMAGING RESOLUTION

1. Resolution factors

The resolution of photoacoustic imaging is primarily limited by the bandwidth of the detector and the laser pulse duration. Theoretically, the structure of tissues with optical absorption contrast can in most cases be either exactly reconstructed or approximately reconstructed by Eq. (4-3). The pressure engaged in the equation is supposed to cover the whole spectrum; and, indeed, the induced photoacoustic signal is rather wide although only part of its spectra can be detected by the single transducer. Using the signals from a limited bandwidth detector causes the reconstructed image to blur. In addition, the reconstructed structure of tissues can also be blurred by the

duration of laser pulse, which is assumed to be a delta stimulation in the derivation of the reconstruction Eq. (4-3). Accordingly, the reconstructed image is affected by the convolution of the structure of tissues in optical absorption, the profile of the pumping pulse, and the impulse response of the detector:

$$I(\mathrm{r}) = S(\mathrm{r}) * L(t \cdot c) * D(t \cdot c)\,, \qquad (4\text{-}4)$$

where, convolution is denoted by *; $I(\mathrm{r})$ characterizes the reconstructed image; $S(r)$ represents the optical structure of tissues; $L(t \cdot c)$ and $D(t \cdot c)$ are the laser pulse and transducer impulse responses converted to the spatial domain. The bell-shaped laser pulse is 6.5 *ns* wide in our experiments and blurs the structure of tissues by ~10 μm.

The effect of an ultrasonic transducer on the detected photoacoustic signals can be investigated by the impulse response. Figure 4-2(a) shows the measured impulse responses accomplished by illuminating the laser pulse onto the transducers and stimulating ultrasonic waves on the surface of the transducers. The effects of the duration of the laser pulse and the limited bandwidth of the ultrasonic transducer are combined in this measurement, which provides a system response. The corresponding spectra are shown in Fig. 4-2(b). Each profile of the impulse responses presents an initial negative lobe, transits to a positive main lobe, and then oscillates to zero.

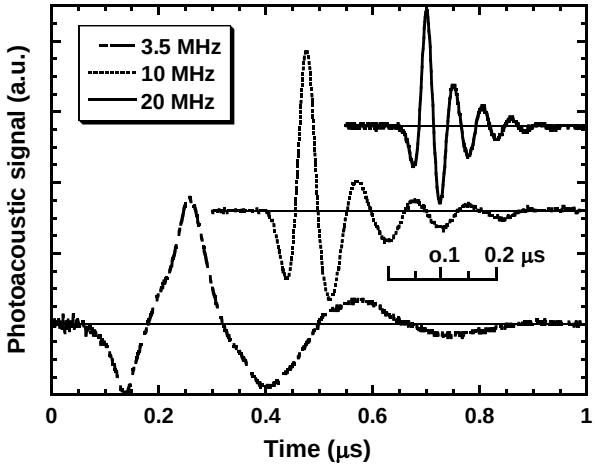

(a)

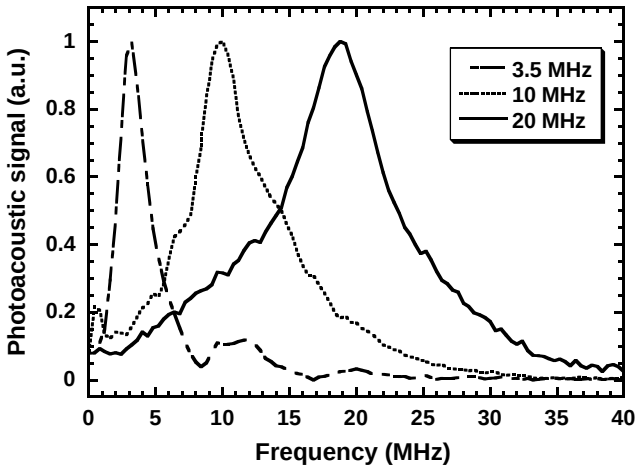

(b)

Figure 4-2. Impulse responses of the ultrasonic transducers stimulated by a laser pulse in (a) the time domain and (b) the frequency domain.

2. Resolution examination

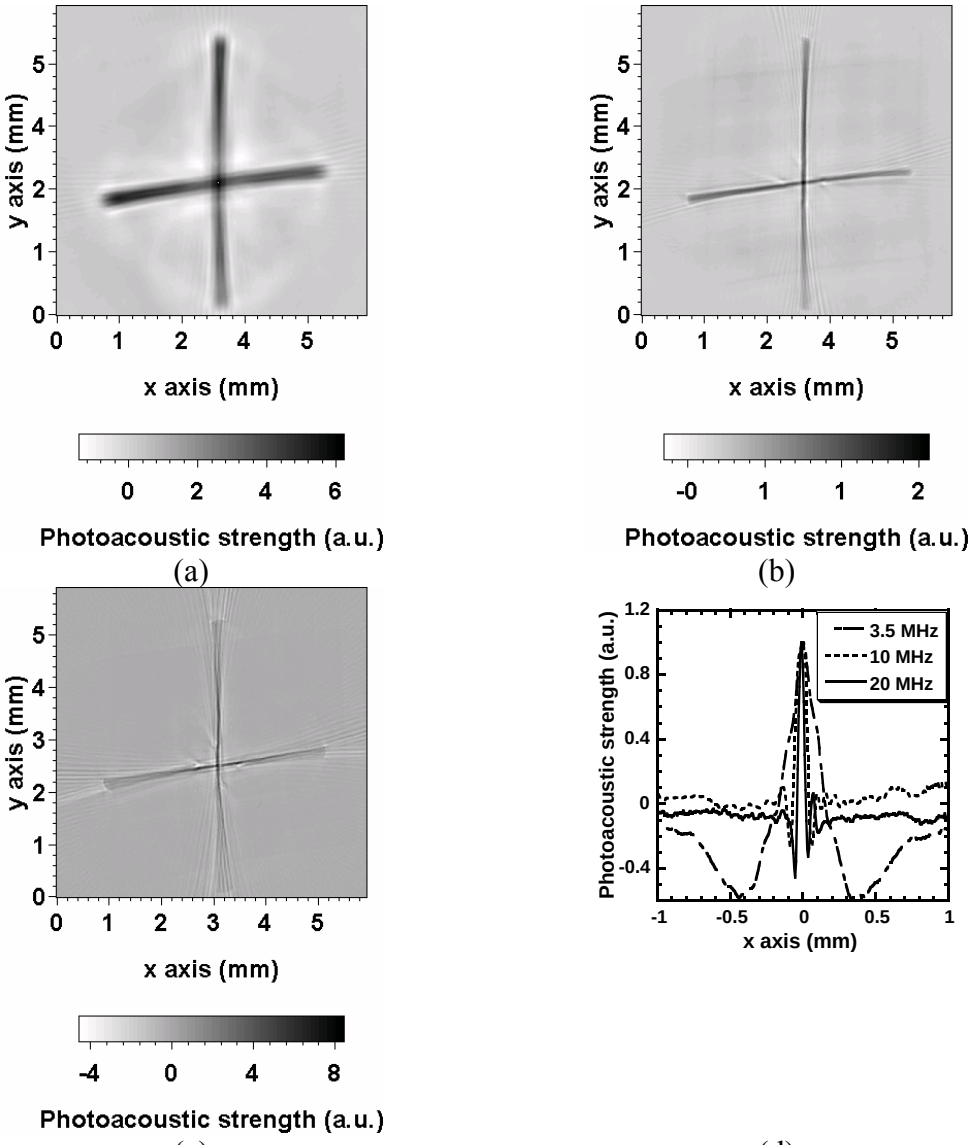

Figure 4-3. Photoacoustic images of a cross made by two mouse hairs acquired with (a) the 3.5-MHz transducer, (b) the 10-MHz transducer, and (c) the 20-MHz transducer. The dark area in the image represents a stronger photoacoustic signal. (d) One-dimensional photoacoustic images of a cross section of the hair fiber of 60 μm in diameter by the three transducers.

To examine the image resolution, we made a phantom sample that is a cross of two mouse hairs in a block of transparent gel (5% gelatin). The photoacoustic images obtained by the three transducers are shown in Figs. 4-3(a)–(c).

Three one-dimensional images of one of the hair fibers, whose diameter is ~60 μm, are plotted in Fig. 4-3(d), where the x axis is shifted to align the peaks. The profile corresponding to the higher frequency transducer is narrower, which indicates higher image resolution. Comparing the reconstructed images in Figs. 4-3(a)–(c) and the one-dimensional images in Fig. 4-3(d), most viewers take the positive main lobe to be the visual object. We here define the resolution of an image as the width of the main lobe crossing zero minus the width of the imaged hair. Here, we checked the image on a cross section of a hair fiber. The zero-crossing widths of the positive main lobes of the reconstructed images are 270 μm, 120 μm and 90 μm for the three transducers — 3.5 MHz, 10 MHz, and 20 MHz, respectively. As discussed in the preceding text, the image of an object is a convolution between the real size of the object and the point spread function of the imaging system. For simplicity, if the diameter of the hair (60 μm) is subtracted from the widths of the main lobes, the corresponding image resolutions appeared to be approximately 210 μm, 60 μm and 30 μm for the above three transducers, respectively. Therefore, an ultrasonic transducer with a higher central frequency and a broader bandwidth generally provides better spatial resolution, which is consistent with the theoretical analysis of the frequency dependence of spatial resolution.[91]

The aperture of the transducer causes its impulse response to be a function of spatial variables. If the aperture is less than the detected ultrasonic wavelength, the

detector approaches a point detector and thus becomes omnidirectional. However, the detector's sensitivity can be augmented by increasing its active areas. The active sizes of the transducers in our experiment are not negligible, consequently, cannot be treated as point detectors; therefore, the impulse responses depend on the position of the photoacoustic source. A heuristic understanding is that the distance between an ultrasonic source in space and a point on the ultrasonic detector with a certain aperture varies with the location of this point on the surface of the detector. This variation causes a variation in the phase of the detected photoacoustic signals which broadens the impulse response. When the transducer scans over the circle, the impulse response remains the same only for the center of the circle. When the ultrasonic source is off the center, the impulse response varies as the ultraducer is scanned. The farther off the ultrasonic source is from the center, the wider the variation of the impulse response. As a result, the image resolution deteriorates with an increase in the distance from the center of rotation. Xu and Wang deduced and predicted this aperture effect mathematically.[91] The aperture effect is obvious in Figs. 4-3(a)–(c), where the hair fibers are clear in the central area of the image, then become broader toward the far ends.

E. PHOTOACOUSTIC IMAGES OF MOUSE BRAIN

The photoacoustic images of a mouse brain obtained by the three ultrasonic transducers are shown in Figs. 4-4(a)–(c), respectively. The images are compared with the open-scalp photograph of the mouse brain shown in Fig. 4-4(d) that was taken after the photoacoustic imaging.

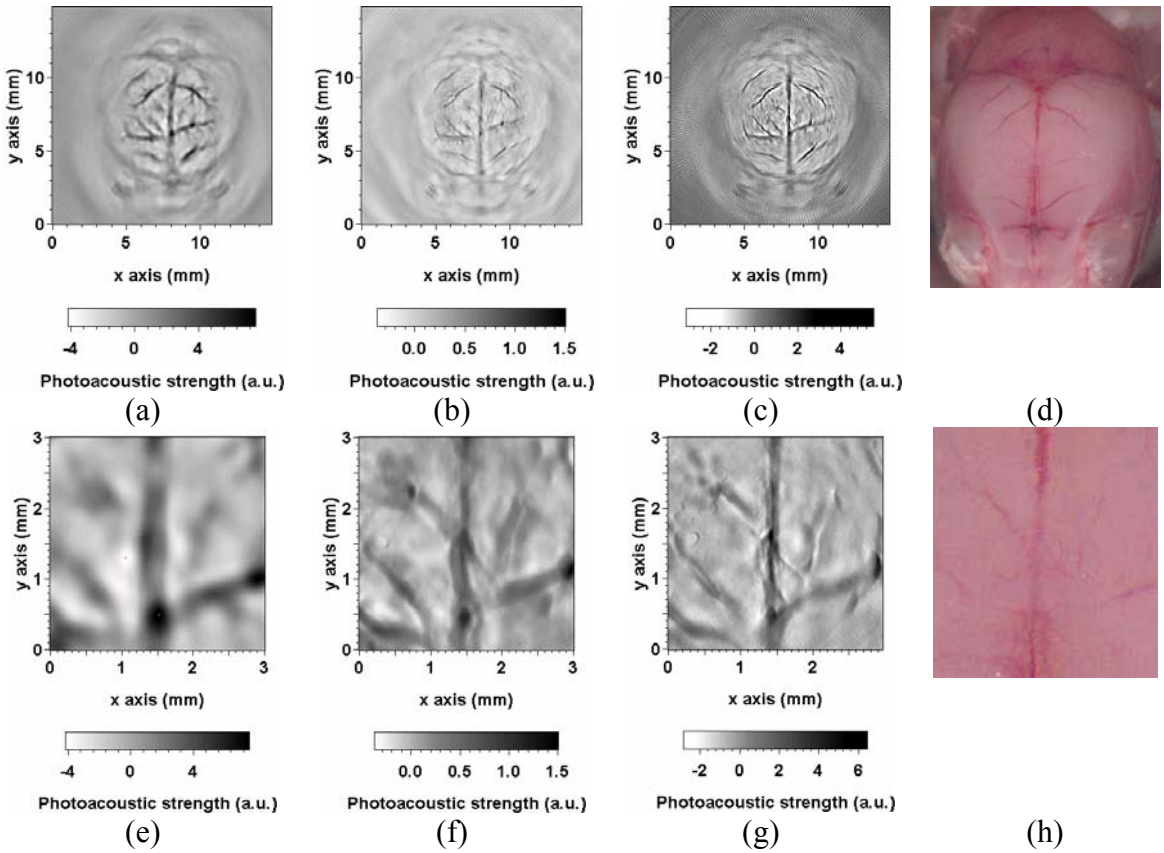

Figure 4-4. Photoacoustic images of a mouse brain acquired with (a) the 3.5-MHz transducer, (b) the 10-MHz transducer, and (c) the 20-MHz transducer. (d) Top-view photograph of the mouse brain where the scalp was stripped after the photoacoustic imaging. (e)–(h) Close-ups of (a)–(d). The dark area in the image represents a stronger photoacoustic signal.

The vessels in the upper cerebral cortex provide the primary photoacoustic source because the laser light is directed to the top of the mouse head and the blood in the vessels has a high optical absorption coefficient at this wavelength. The skull and scalp as well as the other brain tissues around the upper cerebral vessels have much smaller optical absorption coefficients. Light attenuation further reduces the absorbed

optical energy density below the cortex. On the detection side, the photoacoustic sources in the imaging plane are preferentially detected. The diameters of the ultrasonic transducers are greater than their detected ultrasonic wavelengths and cause receiving directionalities; as a result, the effective zone of detection in the imaging area is ~4 mm along the vertical axis. The combined effect of the optical and ultrasonic selectivities produced the clear photoacoustic images of the upper cerebral blood vessels.

By comparing the photoacoustic images with the anatomical photograph, some image properties that correlate with the detection spectra become evident. First, the main vessels on the cortex are disclosed by all three photoacoustic images. The photoacoustic signal covers a broad spectrum and the signal with a limited bandwidth does succeed in recording some of the characteristics of the object regardless of the bandwidth. Secondly, the detected signal from the lower-frequency transducer is stronger, so the SNR of the image is better; but its resolution is poorer. In the image obtained by the 3.5-MHz transducer, every trait shows a feature in the mouse brain although the detailed structure is blurred. Thirdly, higher-frequency detectors provide better image resolution as expected. For an identical vessel, the image obtained by the 3.5-MHz transducer is thicker than those obtained by the other two higher-frequency transducers. The tiny vessels in the central area and some vascular ramifications spreading from the main vessels are perceptible in the image obtained by the 20-MHz transducer but can hardly be seen in the image obtained by the 10-MHz transducer and are totally blurred in the image obtained by the 3.5-MHz transducer. The close-up images reveal the resolution difference more clearly in Figs. 4-4(e)–(h).

The reconstruction improves the SNR of images. The excited ultrasonic signals will appear in the time-dependant signals recorded at all the scanning stops. In the reconstruction algorithm, the received signal amplitude is compensated for by a distance-related factor for each scanning stop. These compensated signals are properly time delayed and summed. For the scanning center and its adjacent area, the summed signal increases approximately by N_s in its amplitude, where N_s is the number of scanning stops. The summed noise increases by only $\sqrt{N_s}$ because of the random characteristic of the noise. So the SNR of the reconstructed image increases approximately $\sqrt{N_s}$ compared with that of a single received ultrasonic signal. If the ultrasonic signal is averaged N_r times, the SNR of the reconstructed image is improved by $\sqrt{N_s N_r}$ in total. In the above experiments, N_s was 240 and N_r was 10 and 50 for the hair imaging and the mouse imaging, respectively. As a consequence, the SNR was improved approximately 49 and 110 times, correspondingly.

CHAPTER V

IMAGING OF TUMOR ANGIOGENESIS IN RAT BRAINS *IN VIVO* BY PHOTOACOUSTIC TOMOGRAPHY

A. PHOTOACOUSTIC IMAGING OF TUMORS

Photoacoustic tomography (PAT) is a non-ionizing imaging modality for visualizing biological tissues with high optical contrast and high ultrasonic resolution. PAT is based on the measurement of laser-induced ultrasonic waves. This imaging modality has contrast similar to that of pure optical imaging and spatial resolution similar to that of pure ultrasonic imaging. Therefore, PAT combines the advantages of two imaging modalities in a single modality.

The laser-induced ultrasonic signals from a biological sample depend on the optical absorption in the sample to reveal the structure of the tissues based on optical contrast. Under the illumination of green laser light at a wavelength of 532 nm, the optical absorption of whole blood is much stronger than that of other tissues: the absorption coefficient of human blood at this wavelength is nearly 200 cm^{-1}, which is almost 10 times higher than that of epidermis and nearly 500 times higher than that of dermis.[27] Therefore, blood generates strong photoacoustic signals and manifests high image contrast, causing the vasculature in organs to stand out prominently in photoacoustic images. Besides the optical absorption, the thermal and elastic properties of the tissues also affect the strength of photoacoustic signals. Therefore, physical

changes, such as density in a tissue, can be reflected in photoacoustic images. The increased density of tumor-bearing tissues is most likely due to a passive mechanism referred to as the "enhanced permeability and retention" effect. In this work, however, we focus solely on the optical contrast that is due to high hemoglobin absorption.

The arrangement of the ultrasonic detector(s) around the region of interest determines the imaging mode and the reconstruction algorithm. For *in vivo* detection of tissue structures under the skin, the ultrasonic transducer can be placed, or scanned, on the skin.[74,75] Hoelen *et al.* realized photoacoustic imaging of vasculature by employing a planar scan of an ultrasonic transducer.[23] Their images, which were reconstructed using a delay-and-sum algorithm, presented depth resolution better than 20 μm and lateral resolution better than 200 μm. A single focused ultrasonic transducer can provide one-dimensional images along the ultrasonic axis, and scanning the transducer linearly over a sample can provide two-dimensional images. In this imaging configuration, the image resolutions are determined by the focal parameters and the bandwidth of the employed ultrasonic detection system.[22,95] Recently, Kolkman *et al.* developed a double-ring detector, which improved the detection directivity, to image veins proximal to the wrist in humans. The feasibility of imaging small deeply embedded tumors was also studied by Esenaliev *et al.* using tissue phantoms.[76] Oraevsky *et al.* used photoacoustic imaging to detect ductal-lobular carcinoma in the breast.[92] Using a single ultrasonic transducer to circularly scan around a small-animal head, Wang *et al.* reconstructed clear photoacoustic images of the cortical vasculature in the brain *in vivo* with high spatial resolution and high optical contrast.[93–95]

Studies in oncology show that angiogenesis, which refers to the formation of new blood vessels within the tumor or the growth of blood vessels between a tumor and its surrounding tissues, plays an important role in tumor growth and metastasis. 96 Angiogenesis constitutes an important control point in the progression of cancer. It has also been proposed that the low metastatic activity of some in situ tumors may be related to their inability to form these new vessels.97,98 There is continued interest in the development of in vivo animal models of brain metastasis to help further the understanding of the mechanisms underlying the spread of tumors and to develop more effective therapies. Unique anatomic and physiologic properties of the brain may invoke special considerations for the design of effective therapies for use against metastases in this organ. Brain-metastatic cells may be sheltered from the effects of some therapeutic agents or immune effector cells by the blood-brain barrier or by specific properties of the brain microenvironment. Furthermore, some of the consequences of treatment-related complications, such as edema or hemorrhage, are more serious in the brain than in other organs. Based on these specific peculiarities of the brain, a noninvasive imaging modality such as PAT is desirable to allow continuous monitoring of the dynamics of the metastatic process and of a tumor therapeutic paradigm on the same animal.

In this chapter, we demonstrate both *ex vivo* and *in vivo* photoacoustic imaging of brain tumors associated with angiogenesis in a rat animal model. All of the photoacoustic images are compared with photographs or the histology of the samples, which are taken after the photoacoustic imaging. To acquire high-quality images with spatial resolutions of various scales, we employee multiple ultrasonic transducers of

different bandwidths to simultaneously scan the rat brain and then reconstruct the images using the data acquired through each transducer independently. The photoacoustic images of both the normal vasculature and the tumor angiogenesis detected by the different bandwidths are compared.

B. EXPERIMENTAL SETUP

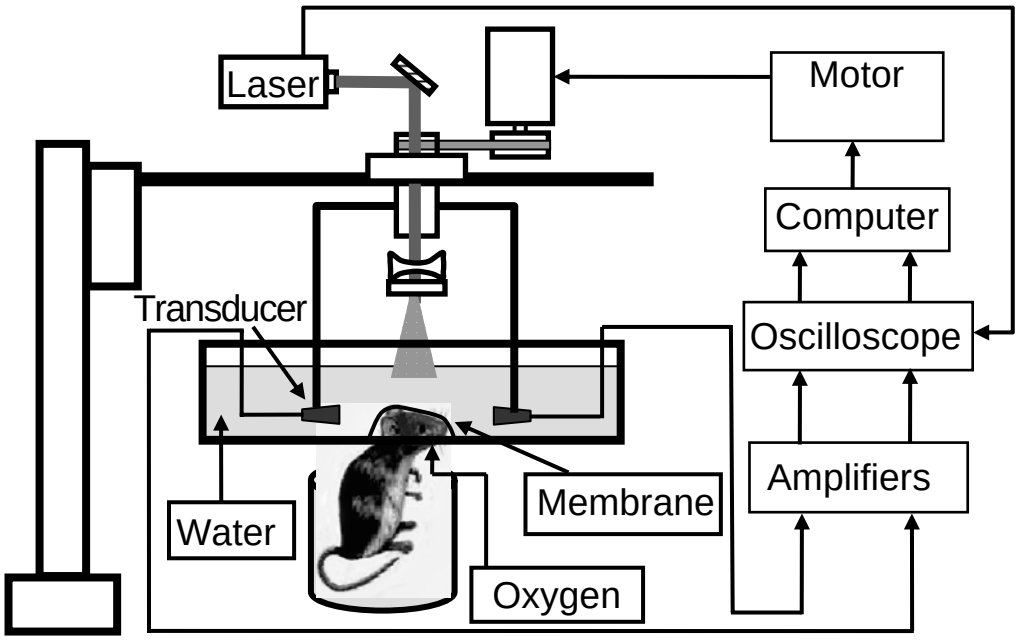

Figure 5-1. Experimental setup of photoacoustic tomography for rat tumor imaging.

The experimental setup of PAT for rat brain tumor detection is shown in Fig. 5-1. The laser light at a wavelength of 532 nm from a Q-switched Nd:YAG laser (Brilliant B, BigSky), operating at the second harmonic wave, is employed as the irradiation source. The laser pulse width is 6.5 ns, and the pulse repetition rate is 10 Hz. The laser beam is

expanded by a concave lens and homogenized by a ground glass to illuminate the rat head from its top. The pulse energy density on the sample surface is controlled to ~20 mJ/cm^2, which is the "maximum permissible exposure" (MPE) for human skin at a wavelength of 532 nm, according to the ANSI standard.[89]

The photoacoustic system has three detection channels that can receive photoacoustic signals through three ultrasonic transducers independently. The ultrasonic transducers (V383, XMS-310, and V316-N, Panametrics) have central frequencies of 3.5 MHz, 10 MHz, and 20 MHz, respectively. The nominal bandwidths of these three transducers are between 50% and 80% of their central frequencies. The diameters of the active areas are 10 mm, 2 mm and 3 mm for the 3.5-MHz, 10-MHz and 20-MHz transducers, respectively. The spatial resolution within the imaging plane appeared to be approximately 210 μm, 60 μm, and 30 μm for the 3.5-MHz, 10-MHz and 20-MHz transducers, respectively.[11] The transducers convert the laser-induced photoacoustic energy into electrical signals. The electrical signals are amplified by amplifiers (ZFL-500LN, Mini-Circuits) and filtered by homemade filters corresponding to the central frequencies and bandwidths of the ultrasonic transducers. An oscilloscope with four channels (TDS-540A, Tektronix) is employed to digitize the three channels of photoacoustic signals simultaneously. A LabView program controls the laser firing, the scanning of the transducers, and the data acquisition.

Each transducer is mounted to a post and connected to a rotational apparatus such that circular scanning in the horizontal plane around the sample can be implemented. The rotational apparatus mounted on a bearing is driven by a step motor (MD-2, Arrick

Robotics). The normal of the active surface of the ultrasonic transducer is aligned to the rotational axis of the circular scanning. We typically complete a full view of a 2π circular scan with 240 steps (1.5°/step). The entire horizontal scanning section is connected to an uprightly placed translation stage. Hence, this section of the system can be manually adjusted vertically to align the scanning plane with the cross section of interest.

For coupling the photoacoustic signals from the sample to the ultrasonic transducer, the transducers are immersed in a tank of water. The rat head is protruded into the water tank through a hole in the bottom of the tank and is insulated from the water by a piece of clear polyethylene membrane covering the hole.

C. SAMPLE PREPARATION

Sprague Dawley rats of 100 to120 grams in body weight are employed in the imaging experiment. General anesthesia is administered to the rat by an intramuscular injection of a mixture of ketamine hydrochloride (44 mg/kg), xylazine hydrochloride (2.5 mg/kg), acepromazine maleate (0.75 mg/kg), and atropine (0.025 mg/kg). The initial anesthesia is maintained as required with an additional half-dose of the intramuscular agents. During the procedure, the rat is placed on a water-circulating heating pad (Gaymar T/pump, Gaymar Industries), and additional heat is provided by an overhead surgical lamp. Before the photoacoustic imaging, the hair on the rat head is removed gently with hair remover lotion. During the data acquisition, pure oxygen is provided to the rat for breathing, and its arterial blood oxygenation (SpO2) level and heart rate are monitored by a pulse oximeter (8600V, Nonin) with the fiberoptic probe

wrapped around the rat's paw. The SpO2 level is near 90%, and the heart rate is close to 350 bpm throughout the experiment, which shows that the rat is in a good condition.

To perform the PAT imaging, a rat animal model that was previously developed by Hall and Stoica was used.[99] The applied rat mammary adenocarcinoma cell line *(Br7-C5)* preferentially metastasizes to the brain when the tumor cells are inoculated via the left ventricle (10^6 cells in 0.2 ml of cultured media). Tumor cells are also transcranially implanted (orthotropic inoculation, 10^5 monodispersed cells) into the brain cortex. One month after the intracerebral inoculation, the experimental rat develops a tumor nodule (around 0.5 cm in diameter) on the cortical surface of the brain, which often protrudes through the skull. The left heart ventricle of the inoculated rat develops neurological clinical signs 40 days post inoculation due to brain metastases development. The histological examination demonstrates that brain metastases are multifocally disseminated within the brain. The inoculation procedures are performed under anesthesia using the ketamine cocktail described above.

D. *EX VIVO* PAT OF RAT BRAIN TUMOR

Photoacoustic images of a tumor-bearing rat brain are acquired *ex vivo* [Fig. 5-2]. On the bottom of Fig. 5-2(a), an open-skull photograph of the rat brain shows a tumor in the cerebellum. The tumor area on the top left of the photograph appears darker than the other parts of the brain cortex. A vibrotome histological section of the tumor, which illustrates tumor hypercellularity and an abundant array of tortuous irregular distorted vessels, is shown on the top of Fig. 5-2(a). The photoacoustic images of the rat

cerebellum detected by the 3.5-MHz and 10-MHz transducers are shown in Figs. 5-2(b) and (c), respectively.

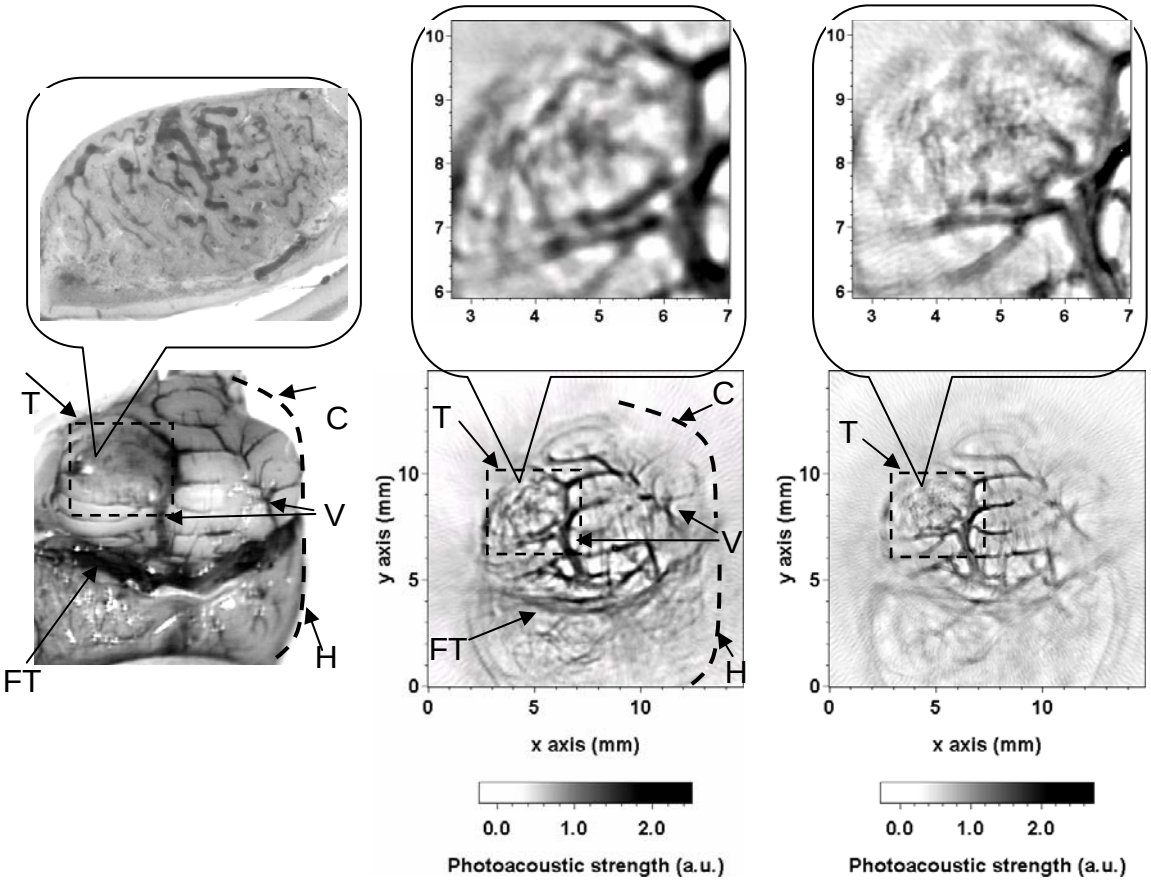

(a) (b) (c)

Figure 5-2. Comparison between a photograph of a tumor-bearing rat brain and the photoacoustic images. (a) Bottom: Photograph of an open-skull rat brain showing a tumor in its cerebrum; Top: Histology of the cerebellar tumor. T, tumor; FT, fissure transversa; C, cerebellum; V, blood vessels; H, partial viewed cerebral hemisphere. Photoacoustic images of the rat brain and the close-up images of the tumor acquired with (b) a 3.5-MHz ultrasonic transducer and (c) a 10-MHz ultrasonic transducer, respectively.

The global images of the brain are shown on the bottom and the corresponding close-up images of the tumor are shown on the top. In our previous PAT experiments, photoacoustic images of tumor-free brains showed well-defined symmetrical vascular architecture in both cortical hemispheres.[10–12] We believe that the detected photoacoustic signals originate primarily from the superficial cerebral veins, sagittal sinus veins, transverse sinus veins and their tributaries, and tumor neovascularization. By comparing the photograph with the photoacoustic images shown in Fig. 5-2, the PAT reveals the vascular architecture associated with the tumorigenesis, which is different from that of a normal brain image. The well-vascularized tumor in the photoacoustic images presents dense dark spots or stripes that represent strong photoacoustic sources from the irregular vessels of angiogenesis, in which the hemoglobin strongly absorbs the laser light. In other words, the normal vascular architecture in the tumor-occupied area is replaced by the newly formed irregular and distorted vessels. The density of the capillaries in the tumor area is also higher than in the normal brain. In summary, tumors exhibit two obvious peculiarities in their vascular structures in the photoacoustic images: the distorted irregular vascular system and the increased density of vessels. The histology confirms that the cerebellar tumor is well-vascularized and the parenchyma hemorrhagic. Both of these factors lead to an increased hemoglobin concentration and subsequently strong photoacoustic signals.

The photoacoustic images acquired with the 3.5-MHz and 10-MHz transducers both show the main vasculature and vessel ramifications with good image quality but with different spatial resolutions. The photoacoustic signal detected by the 3.5-MHz

transducer is stronger; consequently, the corresponding image has a better signal-to-noise ratio and the vascular structure looks more obvious. The image acquired with the 10-MHz transducer has higher image resolution and the subtle vessels are more distinct. Although angiogenesis and distorted vasculature are evident in both the histology and the close-up photoacoustic images, the geometrical shapes of the vessels in the histology differ from those in the photoacoustic images for the following two reasons. First, the orientations of the histologic cross section and the imaged layer are not identical. Secondly, the histology is from a 5 μm thick cross section of the rat brain while the photoacoustic images are from a layer of around 4 mm in thickness.[95]

E. *IN VIVO* PAT OF RAT BRAIN TUMOR

Figure 5-3 presents an *in vivo* photoacoustic image of a living rat with a tumor on its left frontal hemisphere. The photoacoustic image is shown on the left in Fig. 5-3, and a close-up image of the tumor area is shown on the bottom right of Fig. 5-3. After the experiment, the rat is sacrificed and the scalp stripped to compare the anatomy of the rat brain (shown on the top right of Fig. 5-3) with the photoacoustic images.

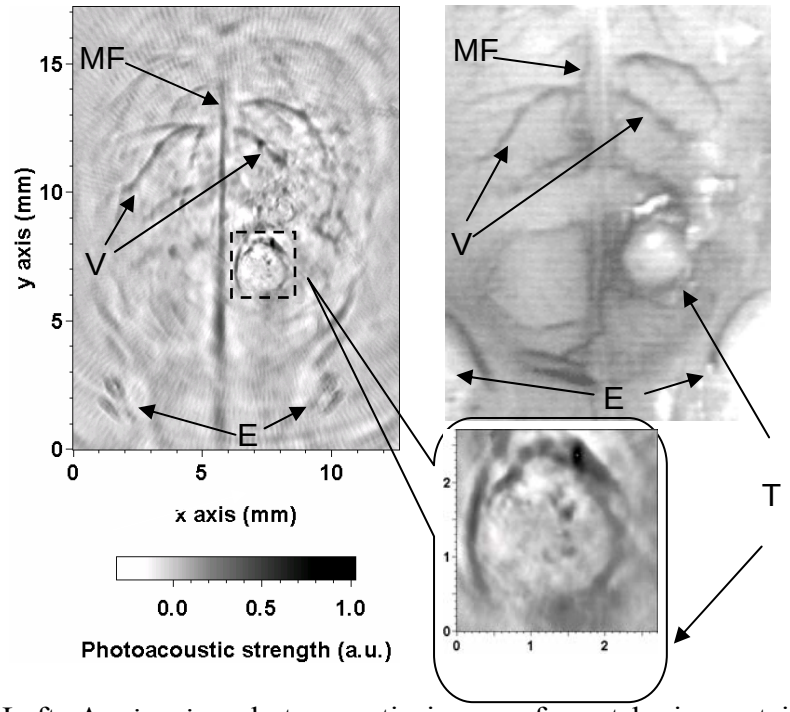

Figure 5-3. Left: An *in vivo* photoacoustic image of a rat brain containing a tumor in its left cerebral hemisphere cortex acquired with a 10-MHz ultrasonic transducer. Bottom right: A close-up photoacoustic image of the tumor. Top right: Photograph of the rat brain through the skull where the scalp was stripped after the photoacoustic imaging. MF, median fissure; V, blood vessels; T, tumor; E, eyes.

The tumor can be easily recognized on the photoacoustic image. In the tumor-free area of the brain cortex, the vessel branches exhibit a normal distribution. However, in the tumor area, the normal vascular architecture is seriously distorted by the growing new blood vessels. The close-up image of the tumor area clearly shows the vascular distortion inside and around the tumor. The developed abnormal vessels due to angiogenesis surround and feed the tumor. This type of tumoral vascular structure under the skin and skull can be clearly imaged non-invasively by PAT.

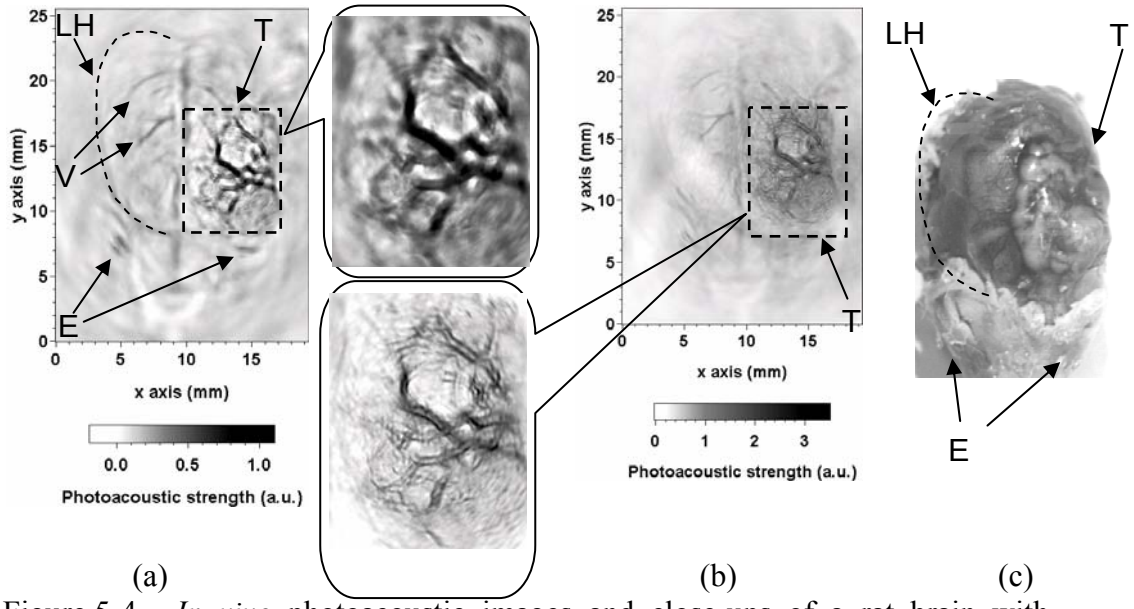

(a) (b) (c)

Figure 5-4. *In vivo* photoacoustic images and close-ups of a rat brain with tumors in the left cerebral hemisphere acquired with (a) a 3.5-MHz ultrasonic transducer and (b) a 20-MHz ultrasonic transducer, respectively. (c) Photograph of the rat brain through the skull where the scalp was stripped after the photoacoustic imaging. LH, left cerebral hemisphere; V, blood vessels; E, eyes; T, tumor.

Figures 5-4(a) and (b) show two *in vivo* photoacoustic images, acquired with the 3.5-MHz and 20-MHz ultrasonic transducers, of another living rat with tumors in its left frontal hemisphere. Two close-up photoacoustic images of the tumors are shown in Fig. 5-4 as well. The images are compared with the open-skull photograph of the rat brain [Fig. 5-4(c)], which was taken after the photoacoustic imaging experiment. In the left frontal hemisphere, the normal vascular distribution was seriously distorted. Besides the tumor- associated irregular and distorted vessels, the hemorrhagic infiltration of

parenchyma is more evident in the tumor area of this rat. Because vessels in developing tumors are more permeable than those in normal tissue, blood can leak into the tumor parenchyma, which also contributes to an increase in optical absorption in the tumor. We attribute the observed photoacoustic imaging patterns to the leaky nature of the tumor vessels, which contain wide interendothelial junctions, an incomplete or absent basement membrane, a dysfunctional lymphatic system, and large numbers of transendothelial channels.[100,101] The photoacoustic images acquired with both the 3.5-MHz and 20-MHz transducers disclose the distorted vasculature associated with the tumorigenesis, but the two images present different characteristics. In the close-up image acquired with the 3.5-MHz transducer, the vessels exhibit solid blurred contours while in the close-up image acquired with the 20-MHz transducer, the vessel contours are better delineated.

CHAPTER VI

DEEP PENETRATING PHOTOACOUSTIC TOMOGRAPHY IN BIOLOGICAL TISSUES

A. PHOTOACOUSTIC IMAGING DEPTH

Photoacoustic tomography (PAT), based on the measurement of laser-induced ultrasonic waves, is a non-ionizing imaging modality for visualizing biological tissues with high optical contrast and high ultrasonic resolution. This imaging modality has been successfully applied to imaging the vasculature structures and tumor angiogenesis a few mm under the skin.[94,96,102] Oraevsky *et al.* studied the imaging sensitivity of PAT on deep embedded objects using tissue phantoms[76] and reported a PAT image of a ductal carcinoma at the depth of 11 mm from the breast surface.[93,103] Due to the overwhelming scattering effect of light in biological tissues, light intensity and hence the photoacoustic signal-to-noise ratio (SNR) decrease exponentially with the depth with a decay constant of a few mm. The light intensity attenuation can be minimized by carefully choosing the excition laser wavelength such that the optical penetration in tissues is maximized. Near-infrared (NIR) has a low absorption coefficient and a relatively low scattering coefficient in biological tissues and can consequently provide deep penetration at the expense of reduced photoacoustic signal strengths. However, photoacoustic signals can be enhanced by using a matched optical contrast agent.[95] Indocyanine green (ICG) has a strong absorption coefficient in the NIR and can serve such a purpose. ICG, in combination with NIR techniques, is widely applied in clinical applications such as

cardiac output monitoring, [104] hepatic function study, [105] angiography in ophthalmology,[106] and tumor detection.[107] In this chapter, we report deep penetrating PAT that was based on an optimal optical wavelength and a matched optical contrast agent. In addition, PAT parameters such as the detection bandwidth and sensitivity were also optimized. We also tested the deep penetrating PAT based on tissue's intrinsic optical contrast. Excited with full power of 1.06 μm NIR, a blood object embedded 5 cm deep in the chicken breast tissue was imaged.

B. EXPERIMENTAL SETUP

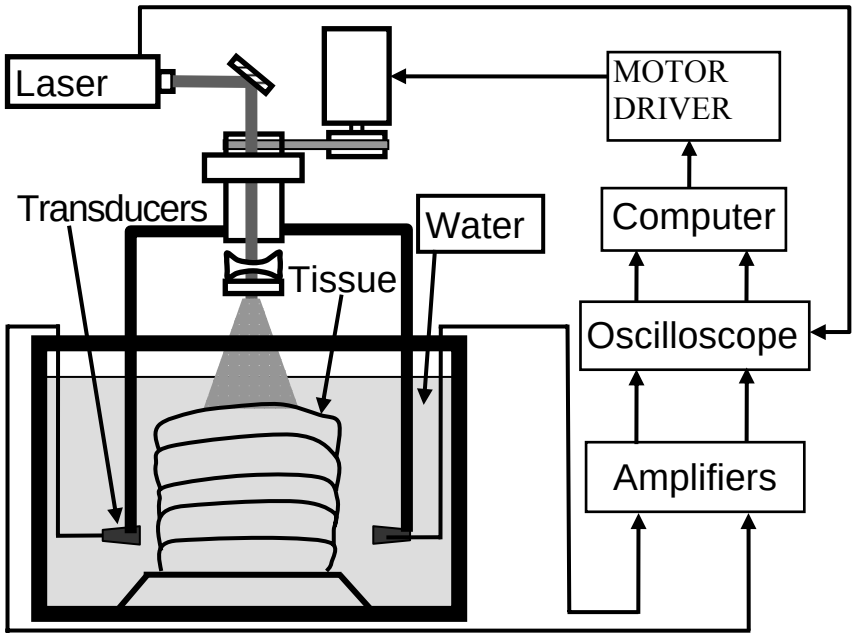

Figure 6-1. Experimental setup of deep penetrating photoacoustic tomography.

In Fig. 6-1, our experimental setup of deep penetrating PAT is shown. A pulse Ti:Sapphire laser (LOTIS TII, Symphotic), which is pumped by a Q-switched Nd:YAG laser, provides 15-ns NIR laser pulses at the wavelength of 800 nm. The laser beam is expanded by a concave lens and homogenized by a ground glass, and then directed onto the sample that was made from chicken breast muscle tissue. The incident laser energy density on the tissue surface is ~7 mJ/cm^2, which is much less than the "maximum permissible exposure" (MPE) of 30 mJ/cm^2 for human skin at this wavelength according to the ANSI standard. The PAT system has four independent detection channels that can receive photoacoustic signals through multiple ultrasonic transducers simultaneously. Four ultrasonic transducers (V323/2.5-MHz, V383/3.5-MHz, V157/5-MHz, and V312/10-MHz, Panametrics), with nominal bandwidths ranging from 50% to 80% of their specified central frequencies, are used for detection in four different frequency ranges. The diameters of their active elements are 0.6 cm, 1 cm, 0.3 cm and 0.6 cm for the 2.25-MHz, 3.5-MHz, 5-MHz and 10-MHz transducers, respectively. The 3.5-MHz transducer is cylindrically focused in the vertical dimension with a focal length of 3.2 cm while the others have flat active surfaces. In response to photoacoustic pressure, the transducers convert the acoustic signals into piezoelectric signals. The signals are subsequently amplified by amplifiers (ZFL-500LN, Mini-Circuits; 5072PR, Panametrics), bandpass filtered by our recently homemade filters, and finally recorded by an oscilloscope (TDS-540A, Tektronix). The sample and transducers are immersed in a tank of water for coupling the photoacoustic waves to the transducers. The transducers are driven by a step motor to scan horizontally along a 10-cm diameter circle

around the sample with a step size of 1.5 degrees. A personal computer is used to control the scanning and data acquisition.

C. DEEP PENETRATING PAT BASED ON EXTRINSIC CONTRAST

1. Sample preparation

Three pairs of transparent plastic tubes of 300 μm in inner diameter each are embedded in chicken breast tissues of ~7.5 cm in diameter in its transverse cross section as shown in Fig. 6-2(a). The first pair of tubes is filled with anticoagulated whole rat blood, the second with ICG solution in distilled water (323 μM), and the last with ICG in rat blood (129 μM). Those centripetally arranged objects are placed in the transducers' scanning plane and covered by chicken breast tissue of various thicknesses as shown in Fig. 6-2(b). For 800 nm NIR light, the optical absorption coefficient is approximately 4-5 cm^{-1} for whole blood, 16 cm^{-1} for the ICG in water and 43 cm^{-1} for the ICG in blood.[108] When excited by laser light, the embedded objects emit photoacoustic waves that propagate through the medium. The photoacoustic signals are picked up by the circularly stationed transducers and fed to image reconstruction based on a back projection algorithm.

2. Deep penetrating PAT in chicken breast tissues

The tissue's cross section containing the embedded objects is imaged when four pieces of chicken breast tissue are sequentially stacked up, which make the embedded objects 1.3 cm, 2.6 cm, 4.2 cm, and 5.2 cm deep from the laser illuminated tissue surface, respectively. Figures 6-2(c) to (f) show the photoacoustic images obtained at

each depth by the 2.25-MHz transducer. A dust grain in the imaging plane is also clearly imaged. The two whole blood columns are liminal at the imaging depth of 1.3 cm, and become unrecognizable when the depth further increases. The ICG solution in water is discernible at the depths up to 5.2 cm. The two ICG-enhanced blood columns have the strongest photoacoustic signals and are clearly imaged throughout. Since the photoacoustic strength is proportional to the absorbed optical energy density in an optical absorber, the photoacoustic signal strengths of the above three kinds of objects at the same depth reflect their differences in the optical absorption. Along the light attenuation direction, the maximum imaging depth is affected by the optical absorption and noise level. On the other hand, increasing the averaging times in the photoacoustic signal acquisition will improve the SNR and make the deeper structures more conspicuous. The laser light intensity decreases almost exponentially with increasing imaging depth. To improve the image quality, we average the photoacoustic signals 50 times at the depth of 1.3 cm, 100 times at 2.6 cm, and 400 times each at 4.2 cm and 5.2 cm.

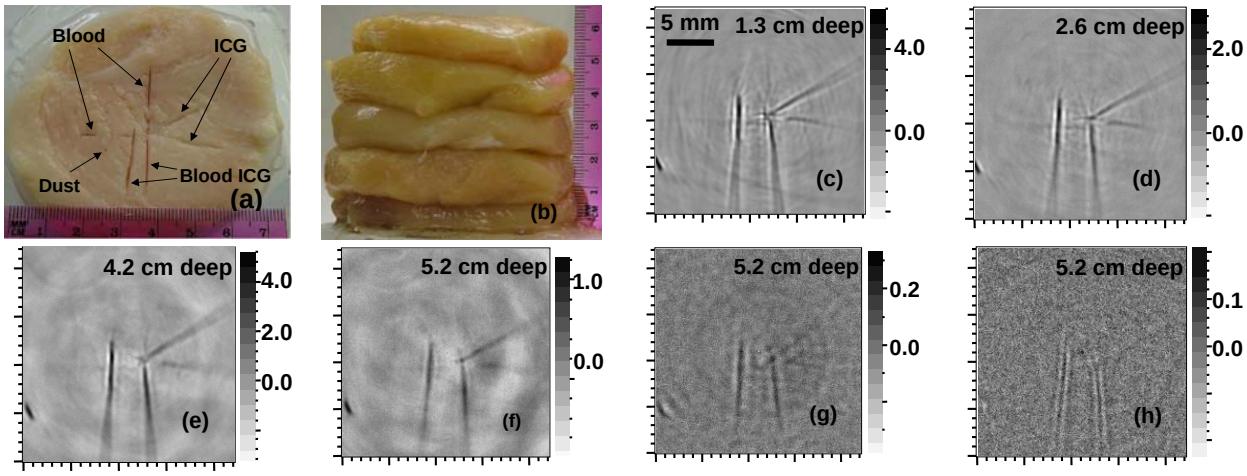

Figure 6-2. Two-dimensional photoacoustic imaging in chicken breast tissues at various depths. (a) Photograph of the imaged cross section of chicken breast tissues in which objects containing blood or ICG or both are embedded. (b) Photograph of the entire sample. Two-dimensional photoacoustic images acquired with a 2.25-MHz ultrasonic transducer at the depths of (c) 1.3 cm, (d) 2.6 cm, (e) 4.2 cm, and (f) 5.2 cm, respectively. Two-dimensional photoacoustic images at a 5.2 cm depth acquired by (g) 3.5-MHz and (h) 5.0-MHz ultrasonic transducers, respectively.

At each depth, four photoacoustic images are simultaneously acquired by the four transducers. Figures 6-2(f) to (h) show the images of the ICG enhanced columns at the 5.2 cm depth by the 2.25-MHz, 3.5-MHz and 5-MHz transducers, respectively. The 10-MHz transducer failed to provide a clear image at this depth. The samples are well delineated in all of the three images, with slight differences in the details, which can be accounted for by the transducers' bandwidth and geometry.[3] The image from the 2.25-MHz transducer has the best SNR whereas the image from the 5.0-MHz transducer provides the sharpest image profile. Because the tubular objects emit more

photoacoustic energy in the lower frequency range, the 2.25-MHz transducer receives stronger signals than the other transducers; in addition, its larger active area helps increasing its detection sensitivity.

The light intensities that transmit through the four tissue thicknesses are detected using a photodiode detector (DET110, Thorlabs) (Fig. 6-3).

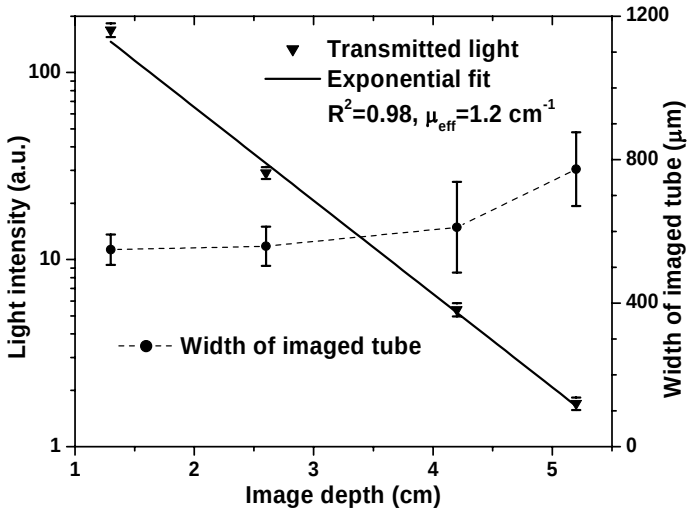

Figure 6-3. Transmitted laser light intensity and width of the blood column in the photoacoustic images acquired by the 2.25-MHz ultrasonic transducer versus the depth of the imaged cross section in the chicken breast tissue.

The effective attenuation coefficient of the chicken breast tissue is fitted to be 1.2 cm^{-1} based on the Beer's law. Therefore, the 5.2-cm maximum imaging depth amounts to approximately 6.2 times the 1/e optical penetration depth, corresponding to a 27-dB attenuation from the incident to the transmitted optical energy density.

The image width of each tube is also examined versus the imaging depth (Fig. 6-3). Inspecting the photoacoustic images at each depth shown in Fig. 2, we first identify the dark imaged columns for the blood with ICG tubes and then calculate the zero-crossing width of the reconstructed image profile across each column as the image width. The variation of the image width reflects the change in the in-plane imaging resolution. The means and variances of the image width within a segment of 5 mm in the central area along the column are calculated. When the tissue thickness increases, the image width remains around 580 μm within the first ~4 cm imaging depth and then becomes wider slowly, increasing to ~780 μm at the depth of 5.2 cm. Therefore, we can conclude that the in-plane spatial resolution is better than 780 μm at the 5.2-cm imaging depth. One can measure the true resolution better with a much smaller object. Theoretically the image resolution is determined by the spectra of the received photoacoustic signals and the SNR. The photoacoustic spectrum, which depends on the excitation laser pulse profile and tissue structures in the imaging plane as well as the detection bandwidth, remains unchanged when the tissue thickness increases. When the SNR is sufficiently high, the resolution is insensitive to the increased tissue thickness. However, when the SNR is low enough to narrow the useful spectrum of the signal above the noise level, the resolution decreases with the increasing tissue thickness. Of course, the off-plane spatial resolution (slice thickness) is determined by the aperture of active element in the ultrasonic transducer if the transducer is unfocused or the numerical aperture if the transducer is focused.

3. ICG sensitivity in deep tissues

We can estimate the sensitivity of our PAT on the detection of ICG based on the ICG concentration and the resolved sample volume. At the 5.2-cm imaging depth, the resolved sample volume is ~(πX0.3^2/4)X0.8 mm^3, where 0.3 mm is the diameter of the tubes and 0.8 mm is the overestimated resolution. Based on the concentration of ICG in the blood ICG mixture, the resolved sample volume contains ~7 pmol of ICG. Of course, the sensitivity is even better at shallower imaging depths. If the incident laser energy density is increased toward the MPE, the sensitivity can be further improved.

4. Deep penetrating PAT in porcine fat tissues

We also imaged blood and ICG objects that were deeply embedded in porcine fat. The photograph in figure 6-4(a) shows the scanning setup for our experiment. Four transducers scan the porcine fat tissues which are located in the center of the container. The photograph of the cross section of porcine fat tissue in which the blood and ICG objects are embedded is shown in Fig. 6-4(b). Those blood and ICG objects are centripetally arranged. The whole blood column is the one located in the lower part of the picture. Two pure ICG solution columns (140 μM/L in water) are on the middle right in the picture. The ICG enhanced blood (14 μM/L of ICG) is the column on the middle left. The top column is the blood extracted from a living rat in which ICG solution had been previously injected intravenously; the ICG concentration in the rat vessels was estimated to be less than 1 μM/L in concentration.

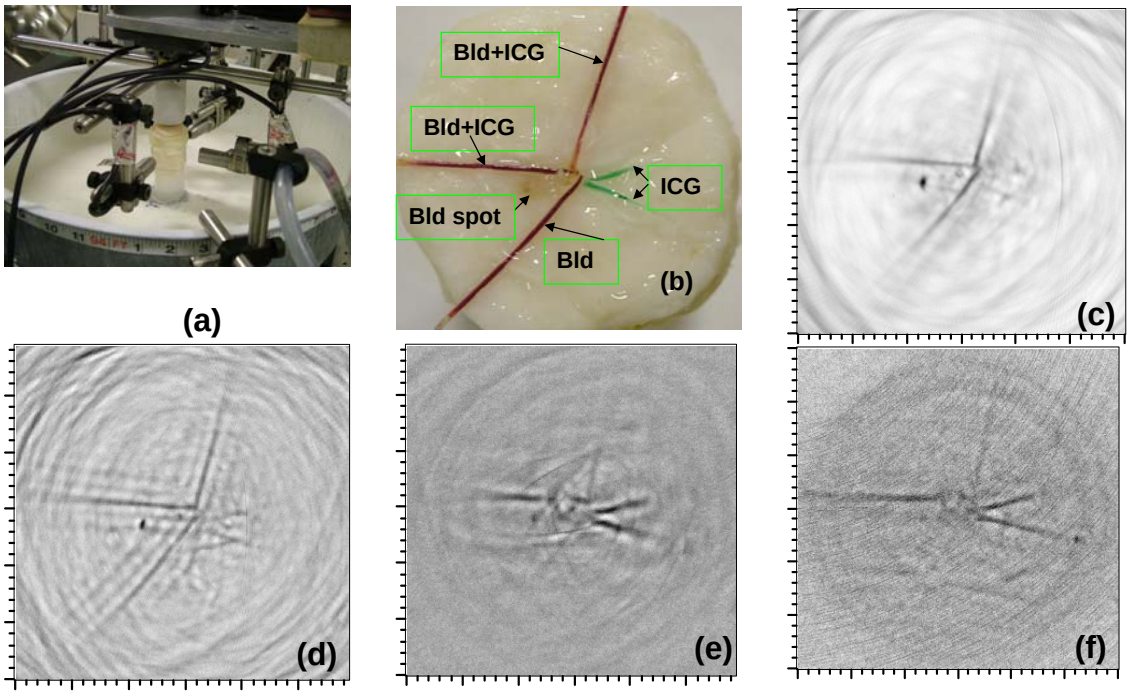

Figure 6-4. Two-dimensional photoacoustic imaging at 2.5 cm depth in porcine fat tissue under the excitation of 532 nm green and 800 nm near infrared light. (a) Photograph of experimental setup, (b) Photograph of the cross section of porcine fat tissue in which blood and ICG objects are embedded. Two-dimensional photoacoustic images under the excitation of 532 nm green laser light acquired with the 10-MHz ultrasonic transducer with a diameter of (c) 10 mm and (d) 2 mm in their active areas, respectively; Two-dimensional photoacoustic images under the excitation of 800 nm near infrared light acquired with the 10-MHz ultrasonic transducer with a diameter of (c) 10 mm and (d) 2 mm in their active areas, respectively.

In the experiment, we first use the green laser light (532 nm in wavelength) as the excitation source. The cross section, where the blood and ICG objects are embedded

2.5 cm away from the laser light illuminated surface, is scanned by four ultrasonic transducers. The PAT images that were simultaneously acquired by two 10-MHz transducers whose active area diameters are 10 mm and 2 mm, respectively, are shown in Fig. 6-4(c) and (d). Because whole blood has a strong (~200 cm^{-1}) absorption coefficient for light of 532 nm in wavelength, the three blood objects are clearly imaged.

An aboriginal nature blood spot in porcine fat tissue on the object plane is clearly imaged between two embedded blood columns in the lower left part of the image. The two columns of pure ICG solution are hardly discernable because of the lower rate of optical absorption of green light. Comparing the two PAT images obtained by the two 10-MHz transducers, the image in Fig. 6-4(c) is cleaner and has better SNR, but the columns rapidly become blurred when the location is farther away from the center, while the blurring in Fig. 6-4(d) occurs more slowly and has a larger image area with satisfactory imaging resolution. This is evidence that the detector with the larger diameter has higher sensitivity in the active area and that the smaller sized detector improves the distribution of the spatial resolution in the imaging area.

Next, instead of green laser light, a NIR of 800 nm in wavelength is employed to induce the photoacoustic signals. The power density on the tissue surface is only 2 mW/cm^2, which is much lower than the ANSI standard of 30 mW/cm^2. Because ICG and ICG enhanced blood have higher rates of optical absorption for a NIR with an 800 nm wavelength, the ICG associated columns are clearly imaged as shown in Fig. 6-4(e) and (f), which were simultaneously acquired by the 10-MHz transducers of 10 mm and 2 mm diameters, respectively, in the active area. The blood extracted from the living rat is

lower in ICG concentration, so its image is weaker than the other ICG columns. The pure blood column and aboriginal blood spot, which are clearly imaged under the green light exciting, are hardly discernable under the weak NIR exciting. Again, the differences between the two images are obvious and confirm the effect of the detector size on the image SNR as well as spatial imaging resolution.

The 1D photoacoustic images crossing one blood column at various imaging depths from 0.5 cm to 2.5 cm are plotted in Fig. 6-5. The y-axis represents the photoacoustic signal strength, and the x-axis shows one image dimension in mm. If we take the positive main lobe as the size of the blood column, the image width is around 650 μm, which is 350 μm greater than the blood column with a diameter of 300 μm. When the imaging depth increases, the photoacoustic strength decreases. At a depth of 2.5 cm, the image is still visible with a good SNR and the image width has not changed significantly compared to those at shallower depths. The imaging resolution is insensitive to the increasing of imaging depth as long as the photoacoustic signal SNR is sufficiently high. In accordance with the attenuation of the photoacoustic strength varying with the imaging depth, the effective attenuation coefficient of the chicken breast tissue is fitted to be 2.5 cm^{-1} based on the Beer's law.

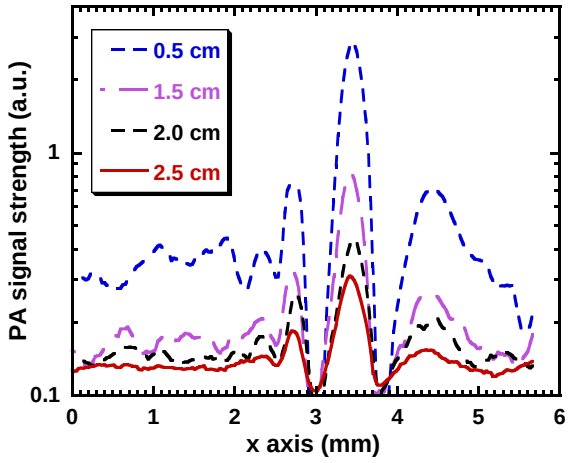

Figure 6-5. One dimensional photoacoustic image crossing one blood column at various imaging depths.

D. DEEP PENETRATING PAT BASED ON INTRINSIC CONTRAST

1. Blood object in porcine fat tissues

Generally, the blood in vasculature has stronger optical absorption than its adjacent tissues. Imaging based on this intrinsic contrast is more attractive and more useful in medical imaging applications.

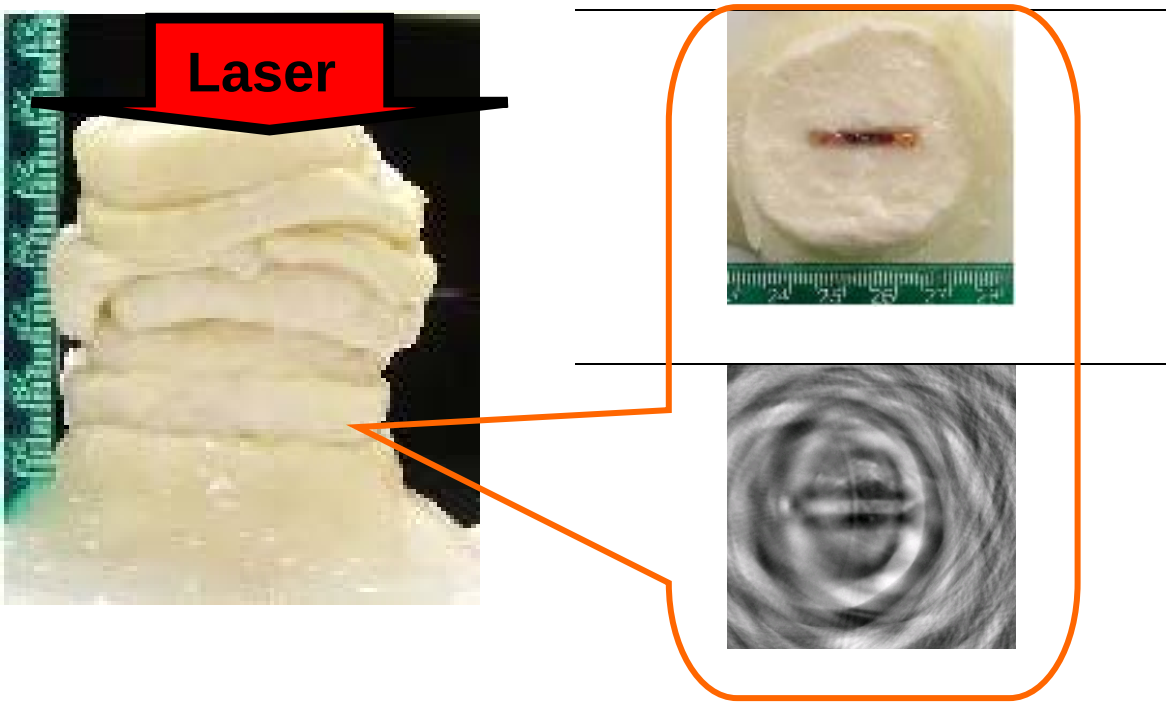

Figure 6-6. Blood sample in porcine fat and its 2D PAT images using a laser light of 1.06-μm wavelength. Left: photograph of the entire sample. Top right: photograph of the imaged cross section of porcine fat in which raw blood is embedded. Bottom right: two-dimensional photoacoustic images acquired with a 2.25-MHz ultrasonic transducer at depths of 5 cm.

The absorption coefficient of whole blood of the infrared light at a wavelength of 1.06 μm is 4 to 5 cm^{-1}. This absorption is less than that of the ICG enhanced blood we used in the experiment described in the part C of this chapter, in which the absorption coefficient is 43 cm^{-1} at a wavelength of 800 nm; but an absorption coefficient of 7 to 8 cm^{-1} is approximately the same as that of the whole blood enhanced by a conservative ICG dosage in some medical applications. In order to image deep vasculature using intrinsic contrast, we chose 1.06 μm laser pulses as the exciting light in our experiment.

This NIR light is deeply penetrating in most biological tissues. Furthermore, the output of the fundamental oscillation from the Nd:YAG laser in our lab can provide full power illumination according to the ANSI standard at a wavelength of 1.06 μm.

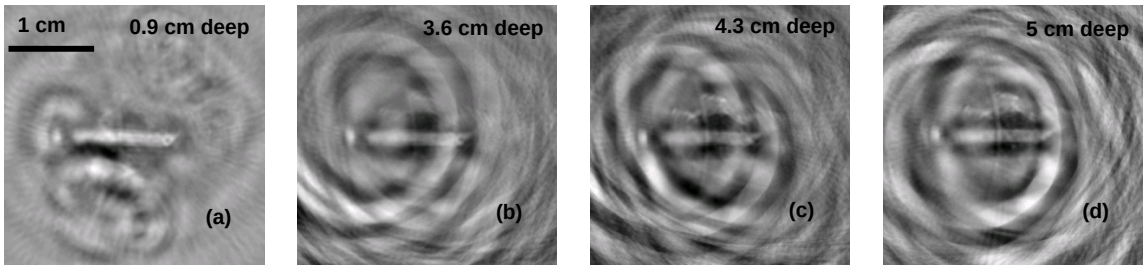

Figure 6-7. Two-dimensional photoacoustic images of blood object in porcine fat acquired with a 2.25-MHz ultrasonic transducer at depths of (a) 0.9 cm, (b) 3.6 cm, (c) 4.3 cm, and (d) 5 cm, respectively.

Using NIR laser pulses at the 1.06 μm wavelength, we image the blood object embedded in porcine fat tissues as shown in Fig. 6-6. Seven pieces of porcine fat tissues were sequentially stacked up to increase the imaging depth as shown in the left picture in Fig. 6-6. Laser light illuminates the test sample from its top. The object was made by pouring raw rat blood into a transparent plastic tube with a diameter of 1.5 mm and embedding it in the porcine fat tissues. The photograph of the blood object embedded cross section is on the top right of Fig. 6-6. The PAT image of the blood object at a depth of 5 cm is shown on the bottom right. As each porcine fat sample was added, the blood embedded cross section of the porcine fat tissues is simultaneously scanned by four transducers. The PAT images at depths of 0.9 cm, 3.6 cm, 4.3 cm and 5 cm

achieved by 2.25-MHz transducer and 3.5-MHz transducer are shown in Fig. 6-7(a) to (d) and Fig. 6-8(a) to (d), respectively.

The blood object is imaged clearly at the depth of 0.9 cm. In porcine fat, there are some aboriginal nature vessels or other optical absorbing tissues, which absorb laser energy and generate photoacoustic signals. When the absorbers are located above the transducers' scanning plane, (in which blood object is embedded), and near the laser illuminated surface, more laser energy will be absorbed and stronger photoacoustic signals will be generated. Since the photoacoustic sources are not seated in the horizontal imaging plane, they are blurred in the reconstructed images, in which the blood column is well focused. The farther the aboriginal nature absorbers are away from the scanning plane, the more they are blurred and they even presented some circles in the image. According to the radius of the circles on the PAT images, those interferences were estimated coming from the location near the laser illuminated tissue surface. When the imaging depth increases, the interference becomes more obvious and meddlesome in the image, and the embedded blood object can only be recognized from its geometrical shape. This phenomenon is obvious in the images obtained by the flat transducer (2.25-MHz, 6 mm in diameter) shown in Fig. 6-7.

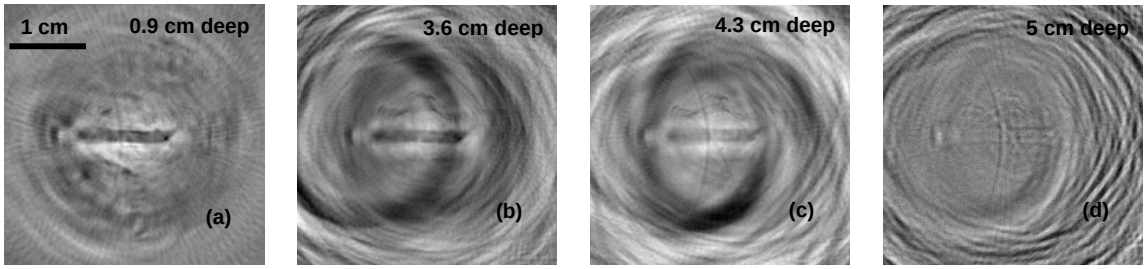

Figure 6-8. Two-dimensional photoacoustic images of a blood object in porcine fat acquired with a 3.5-MHz ultrasonic transducer at depths of (a) 0.9 cm, (b) 3.6 cm, (c) 4.3 cm, and (d) 5 cm, respectively.

In the images detected by the horizontally cylindrically focused transducer (3.5-MHz, 10 mm in diameter) shown in Fig. 6-8, the interference is not serious because the signals generated from the induced photoacoustic sources beyond the focal zone of the detector are cancelled out. The images shown in Fig. 6-8 are cleaner than those in Fig. 6-7. When the imaging depth increases to 5 cm, the blood column becomes obscure but still discernible.

The laser power density at the tissue surface was measured to be 630 mW/cm^2 at a wavelength of 1.06 μm. The laser light transmitted through the tissues was also measured using a power meter (SmartSensor 30V, Coherent). The photoacoustic signal is proportional to the laser light intensity; therefore, the photoacoustic signal amplitude can be used to scale the light attenuation. The effective attenuation coefficient of the porcine fat tissue is fitted to be around 2.5 cm^{-1} and 2.1 cm^{-1} according to both the transmitted light power measurement and the photoacoustic signal attenuation. Therefore, the 5 cm imaging depth is approximately 10 times the 1/e optical penetration depth, corresponding to 43-dB attenuation from the incident to the transmitted optical

energy density. The optical properties of human breast tissue were examined for different of human groups. Ths effective optical attenuation rabge varies widely, but a typical value is around 0.22 cm^{-1} at NIR.[17] The following table shows some optical measurements of the human breast tissues at NIR light.[109]

Table 6-1. Human breast optical properties in near infrared light

Wavelength(nm)	μ_a (cm-1)	μ_s'(cm-1)	μ_{eff} (cm-1)	δ (cm)
754	0.046	8.9	1.1	0.9
800	0.017-0.045	7.2-13.5	0.7	1.36
749	0.18	8.48	2.16	0.46
700	0.7	8.6	4.4	0.23

2. Blood object in chicken breast tissues

Chicken breast tissue is considered to have an effective optical attenuation coefficient that is similar to that of human breast tissue. Deep penetrating PAT was also tested on chicken breast tissues of around 7 to 8 cm in transversal dimensions. Raw blood in transparent plastic tube was buried as object as shown in Fig. 6-9.

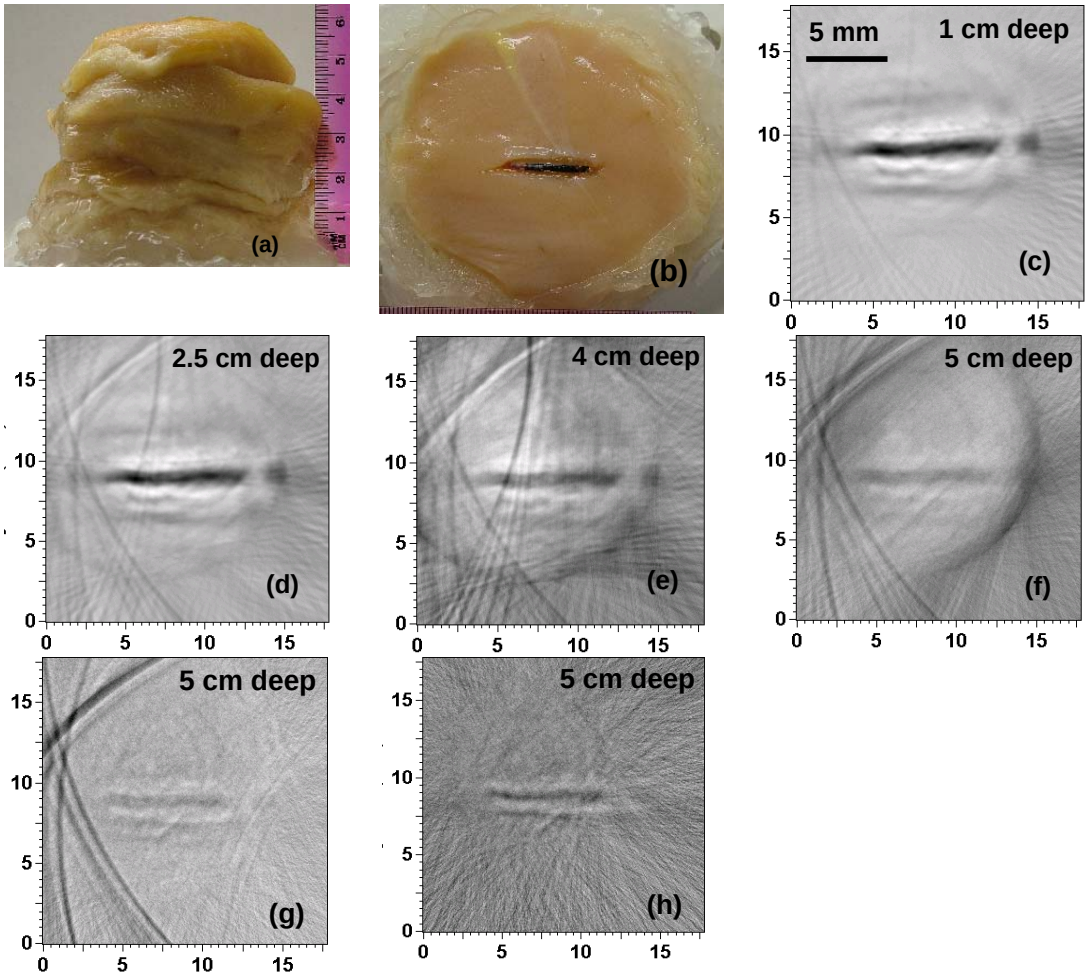

Figure 6-9. Two-dimensional photoacoustic imaging at various depths. (a) Photograph of the entire sample, (b) Photograph of the cross section of chicken breast tissue in which a blood object is embedded. Two-dimensional photoacoustic images acquired with a 3.5-MHz ultrasonic transducer at depths of (c) 1 cm, (d) 2.5 cm, (e) 4 cm, and (f) 5 cm, respectively. Two-dimensional photoacoustic images at a 5 cm depth improved by (g) an optimized bandpass filter and (h) post data processing, respectively.

The photograph of the entire sample and the object embedded cross section are shown in Fig. 6-9(a) and (b), respectively. Similar to the previous experiments, the

tissue's cross section containing the embedded blood object is imaged when four pieces of chicken breast tissues are sequentially stacked up, which placed the embedded objects 1 cm, 2.5 cm, 4 cm, and 5 cm, respectively, away from the laser illuminated tissue surface. Figures 6-9(c) to (f) show the photoacoustic images acquired by the 3.5-MHz transducer at each depth. The blood object is clearly imaged when it is 1 cm and 2.5 cm below the laser illuminated surface. At a depth of 4 cm, the blood column is still clearly visible although there is some interference muddying the image. When the forth chicken tissue sample of 1 cm in thickness was stacked on, making the blood object 5 cm deep, the blood object becomes obscured. Checking the photoacoustic images of the blood column at each depth, the image width retains clarity at around 2 mm at a depth of less than 4 cm and increases a little bit in a depth of 5 cm because of image blurring. In the longitudinal direction, there is a dark spot lying away from the right end of the blood column in the imaged. We discovered later that there was a bubble at the corresponding position inside the tube, which separated the blood column into two parts. This sample fault is clearly revealed by the photoacoustic imaging.

Photoacoustic images can be improved by choosing the optimal detection bandwidth and proper data processing. The detection electronics determine the effective SNR which is very important to the image quality. In the experiment, several bandpass filters associated with the amplifiers are tested after carefully studying the spectra of the photoacoustic signals from the object, the unexpected interference from the other optical absorbers, and the system noise. Figure 6-9(g) shows the photoacoustic image which is improved by this optimized hardware. Comparing the images acquired under the same

experimental conditions but with a slight difference in filters and amplifiers, the later image is improved in SNR and some interference is removed. There is also an opportunity to improve the photoacoustic image further by post experiment data processing. We can find a trace of an expected signal or unexpected interference on the measurement sonogram or spectra, and then use digital filters or time gating to reduce the unexpected inference and improve the image quality. Figure 6-9(h) shows the result of the data processing, in which the interference is completely removed and the blood object is clearly presented.

CHAPTER VII

SUMMARY AND CONCLUSIONS

Employing ultrasonic transducers of various bandwidths, two-dimensional photoacoustic tomography successfully reveals the vascular structures of the cortex in the mouse brain with various traits. We demonstrated that a higher-frequency ultrasonic transducer gives a higher resolution image while a lower-frequency transducer provides images with a higher signal-noise ratio. The image resolutions appeared to be approximately 210 μm, 60 μm and 30 μm for the transducers of 3.5 MHz, 10 MHz, and 20 MHz, respectively. In clinical imaging applications, tumors and other tissues are likely to have complicated shapes and optical absorptions. Consequently, the acoustic signals will have wide spectra. It will be difficult to set the detection bandwidth optimally in advance. The use of multiple transducers, each differing in the central frequency, is a superior method for capturing the images which cover a wide spectrum.

PAT can be used to detect tumors in rat brains by imaging the tumor-related vasculature and tumor parenchymal imbibition of blood. The image resolution and contrast are good enough to resolve the vessels in the brain; therefore, a tumor associated with angiogenesis can be diagnosed reliably. PAT is suitable for monitoring tumor growth, angiogenesis and anti-angiogenic therapy in experimental carcinogenesis on animal models. This non-invasive technology allows for monitoring the same animal at multiple time points as well as reducing the individual variability and the number of experimental animals required.

Three aspects of PAT are optimized to image deep tissue structures. Firstly, NIR laser, which has deep penetration in biological tissues light, is employed as an exciting source; secondly, an optical contrast agent, ICG, is applied to enhance the optical absorption of blood; thirdly, multiple ultrasonic transducers are simultaneously used to balance the detection sensitivity and image resolution. It is demonstrated that fine blood-containing tubes embedded at a greater than 5-cm depth in chicken breast tissue can be clearly imaged with a better than 780-μm resolution using PAT. These results suggest that non-ionizing PAT can potentially image deep vasculatures in the breast and other organs. Our experimental data also implies that PAT can potentially image blood associated tissue structures using intrinsic tissue contrast.

We have investigated scanning microwave-induced thermoacoustic tomography both experimentally and theoretically. Our theoretical analysis of SNR showed that for malignant tissue located at a 3-6 cm depth, the choice of the optimal microwave frequency is broad, ranging between 100 MHz and 3 GHz. The axial resolution was obtained by measuring the time-resolved microwave-induced thermoacoustic signals. Depth-resolved tomographic images were acquired directly without resorting to computational image reconstruction. The key factors affecting the axial resolution include the pulse width of microwave and the bandwidth of the ultrasonic transducer. The lateral resolution is achieved by the use of a focused ultrasonic transducer. The factors affecting the lateral resolution include the numerical aperture of the ultrasonic transducer and the central frequency of the piezoelectric signal in response to the thermoacoustic wave. The central frequency of the piezoelectric signal is determined by

the frequency response of the ultrasonic transducer and the frequency spectrum of the microwave-induced thermoacoustic wave in the resolvable dipolar structures. Gain compensation can counteract the microwave attenuation and improve the image contrast.

REFERENCES

[1] A. G. Bell, Am. J. Sci. **20**, 305 (1880).

[2] A. C. Tam, Rev. Mod. Phys. **58**, 381 (1986).

[3] A. Rosencwaig, *Photoacoustics and Photoacousic Spectroscopy* (Wiley, New York, 1980).

[4] C. K. N. Patel and A. C. Tam, Rev. Mod. Phys. **53**, 517 (1981).

[5] G. A. West, J. J. Barrett, D. R. Siebert, and K. V. Reddym, Rev. Sci. Instrum. **54**, 797 (1983).

[6] D. A. Hutchins and A. C. Tam, IEEE Trans. Ultrason. Ferroelectr. Freq. Control. **33**, 429 (1986).

[7] M. W. Sigrist, J. Appl. Phys. **60**, R83 (1986).

[8] V. P. Zharov, V. S. Letokhov, *Laser Optoacoustic Spectroscopy*, Springer Series in Optical Science, Vol. 37 (Springer-Verlag, New York, 1986).

[9] K. H. Michaelian, *Photoacoustic Infrared Spectroscopy* (Wiley-Interscience, Hoboken, New Jersey, 2003).

[10] *Principles and Perspectives of Photothermal and Photoacoustic Phenomena*, edited by A. Mandelis (Elsevier Science, New York, 1992).

[11] J. M. Chalmers and P. R. Griffiths, eds., *Handbook of Vibrational Spectroscopy* (John Wiley & Sons, New York, 2002).

[12] V. E. Gusev and A. A. Karabutov, *Laser Optoacoustics* (AIP, New York, 1993).

[13] A. A. Oraevsky, ed., *Biomedical Optoacoustics*, Proc. SPIE **3916** (SPIE, Bellingham, Washington, 2000).

[14] A. A. Oraevsky, ed., *Biomedical Optoacoustics II*, Proc. SPIE **4256** (SPIE, Bellingham, Washington, 2001).

[15] A. A. Oraevsky, ed., *Biomedical Optoacoustics III*, Proc. SPIE **4618** (SPIE, Bellingham, Washington, 2002).

[16] A. A. Oraevsky, ed., *Biomedical Optoacoustic IV*, Proc. SPIE **4960** (SPIE, Bellingham, Washington, 2003).

[17] F. A. Duck, *Physical Properties of Tissue*, (Academic, London, 1990).

[18] W. F. Cheong, S. A. Prahl and A. J. Welch, IEEE J. Quantum Elect. **26**, 2166 (1990).

[19] L. E. Larsen and J. H. Jacobi, *Medical Applications of Microwave Imaging* (IEEE, New York, 1986).

[20] P. M. Meaney, M. W. Fanning, D. Li, S. P. Poplack and K. D. Paulsen, IEEE Trans. Microwave Theory Tech. **48**, 1841 (2000).

[21] R. A. Kruger, D. R. Reinecke, and G. A. Kruger, Med. Phys. **26**, 1832 (1999).

[22] G. Ku, L.-H. Wang, Med. Phys., **27**, 1195 (2000).

[23] C. G. A. Hoelen, F. F. M. Demul, R. Pongers, and A. Dekker, Opt. Lett. **23**, 648 (1998).

[24] A. A. Oraevsky, S. L. Jacques, R. O. Esenaliev, and F. K. Tittel, "Laser-based optoacoustic imaging in biological tissues," in *Laser-Tissue Interaction V,* S. L. Jacques, eds., Proc. Soc. Photo-Instrum. Eng. **2134A**, 122-128 (1994).

[25] C. C. Johnson and A. W. Guy, Proc. IEEE **60**, 692 (1972).

[26] K. R. Foster, IEEE Trans. Plasma Sci. **28**, 15 (2000).

[27] S. L. Jacques and S. A. Prahl, http://omlc.ogi.edu/classroom/ece532/class3/muaspectra.html (2004).

[28] P. N. T. Wells, Rep. Prog. Phy. **62**, 671 (1999).

[29] L. Pan, Ultrasound in Med. & Biol. **24**, 995 (1998).

[30] C.M.W Daft, J. Acoust. Soc. Amer. **85** 2195 (1989).

[31] F. S Foster, Ultrasound in Med. & Biol. **26**, 1 (2000).

[32] G. J. Diebold, T. Sun, and M. I. Khan, Phys. Rev. Lett. **67**, 3384 (1991).

[33] J. D. Jackson, *Classical Electrodynamics*, 2nd ed. (John Wiley & Sons, New York, 1999).

[34] G. B. Arfken and H. J. Weber, *Mathematical Methods for Physicists*, 4th ed. (Academic, San Diego, California, 1995).

[35] P. M. Morse and H. Feshbach, *Methods of Theoretical Physics* (McGraw-Hill, New York, 1953).

[36] P. M. Morse and K. U. Ingard, *Theoretical Acoustics* (McGraw-Hill, New York, 1968).

[37] V. E. Gusev, and A. A. Karabutov, *Laser Optoacoustics* (AIP, New York, 1993).

[38] I. N. Bronshtein, K. A. Semendyayev, *Handbook of Mathematics* (Van Nostrand Reinhold, New York, 1978).

[39] G. J. Diebold, and T. Sun, Acoustica, **80** 339 (1994).

[40] L. E. Larsen and J. H. Jacobi, *Medical Applications of Microwave Imaging* (IEEE, New York, 1986).

[41] J. C. Lin, Proc. of IEEE **73**, 374 (1985).

[42] S. Caorsi, A. Frattoni, G. L. Gragnani, E. Nortino, and M. Pastorino, Med. Biol. Eng. Comput. **29**, NS37 (1991).

[43] M. S. Hawley, A. Broquetas, L. Jofre, J. C. Bolomey, and G. Gaboriaud, J. Biomed. Eng. **13**, 197 (1991).

[44] P. M. Meaney, K. D. Paulsen, and J. T. Chang, IEEE Trans. Microwave Theory Tech. **46**, 31 (1998).

[45] J. C. Lin, IEEE Trans. Microwave Theory Tech. **25**, 605 (1977).

[46] F. Caspers and J. Conway, in *Proc. of the 12th European Microwave Conference*, 565 (1982).

[47] J. L. Su and J. C. Lin, IEEE Trans. Biomed. Eng. **43**, 178 (1987).

[48] J. S. K. Wan, Res. Chem. Intermed. **19**, 147 (1993).

[49] T. Bowen, L. Nasoni, A. E. Pifer, and G. H. Sembrosk, in *Proc. IEEE Ultrasonics Symposium* **2**, 823 (1981).

[50] J. P. Powers, ed., *Acoustic Imaging* (Plenum Publishing, New York, 1982).

[51] R. G. Olsen and J. C. Lin, Bioelectromagnetics **4**, 397 (1983).

[52] J. C. Lin and K. H. Chan, IEEE Trans. Microwave Theory Tech. **32**, 854 (1984).

[53] R. L. Nasoni, G. A. Evanoff Jr., P. G. Halverson, and T. Bowen, in *Proc. IEEE Ultrasonics Symposium* **5**, 633 (1984).

[54] K. H. Chan and J. C. Lin, in *Proc. Engineering in Medicine and Biology Society 10th Annual International Conference*, 445 (1988).

[55] R. A. Kruger, K. K. Kopecky, A. M. Aisen, D. R. Reinecke, G. A. Kruger, and W. L. Kiser Jr., Radiology **211**, 275 (1999).

[56] L. V. Wang, X. Zhao, H. Sun, and G. Ku, Rev. Sci. Instrum. **70**, 3744 (1999).

[57] R. A. Kruger and P. Liu, Med. Phys. **21**, 1179 (1994).

[58] A. A. Oraevsky, R. Esenaliev, F. K. Tittel, M. R. Ostermeyer, L.-H. Wang, and S. L. Jacques, Laser-Tissue Interaction VII **2681**, 277 (1996).

[59] R. O. Esenaliev, H. Alma, F. K. Tittel, and A. A. Oraevsky, in *Laser-Tissue Interaction IX,* S. L. Jacques, eds., Proc. Soc. Photo-Instrum. Eng. **3254**, 294 (1998).

[60] A. A. Oraevsky, V. A. Andreev, A. A. Karabutov, and R. O. Esenaliev, in *Laser-Tissue Interaction X: Photochemical, Photothermal, and Photomechanical,* S. L. Jacques, G. J. Mueller, A. Roggan, and D. H. Sliney, eds., Proc. SPIE **3601**, 256 (1999).

[61] C. G. A. Hoelen, F. F. M. de Mul, and J. Greve, Proc. SPIE **2628,** 308 (1995).

[62] A. O. Oraevsky, S. L. Jacques, and F. K. Tittel, Appl. Opt. **36**, 402 (1997).

[63] C. Gabriel, S. Gabriel, and E. Corthout, Phys. Med. Biol. **41**, 2231 (1996).

[64] S. Gabriel, R. W. Lau, and C. Gabriel, Phys. Med. Biol. **41**, 2251 (1996).

[65] S. Gabriel, R. W. Lau, and C. Gabriel, Phys. Med. Biol. **41**, 2271(1996).

[66] C. C. Johnson, A. W. Guy, Proc. IEEE, **60**, 692 (1972).

[67] S. Chaudhary, R. Mishra, A. Swarup, and J. Thomas, Indian Journal of Biochemistry and Biophysics **21**, 76 (1984).

[68] K. R. Foster and J. L. Schepps, J. Microwave Power **16**, 107 (1981).

[69] W. Joines, R. Jirtle, M. Rafal, and D. Schaeffer, Radiation Oncology-Biology-Physics **6**, 681 (1980).

[70] W. Joines, Y. Zhang, C. Li, and R. Jirtle, Med. Phys. **21**, 547 (1994).

[71] A. A. Oraevsky, V. A. Andreev, A. A. Karabutov, D. R. Fleming, Z. Gatalica, H. Singh, and R. O. Esenaliev, *Proc. SPIE,* **3597**, 352 (1999).

[72] S. J. Nelson, and C. Soonmee, Journal of Cancer*,* vol. **9**, 134 (2003).

[73] A. A. Karabutov, E. V. Savateeva, N. B. Podymova, and A. A. Oraevsky, J. Appl. Phys. **87**, 2003 (2000).

[74] A. A. Karabutov, E. V. Savateeva, and A. A. Oraevsky, in *Laser-Tissue Interaction X: Photochemical, Photothermal, and Photomechanical,* S. L. Jacques, G. J. Mueller, A. Roggan, and D. H. Sliney, eds., Proc SPIE **3601**, 284 (1999).

[75] R. O. Esenaliev, A. A. Karabutov, and A. A. Oraevsky, IEEE J. Sel. Top. Quant. **5**, 981 (1999).

[76] R. O. Esenaliev, F. K. Tittel, S. L. Thomsen, B. Fornage, C. Stelling, A. A. Karabutov, and A. A. Oraevsky, Proc. SPIE **2979**, 71 (1997).

[77] C.G.A. Hoelen, and F. F. M. de Mul, Appl. Opt. **39**, 5872 (2000).

[78] R. A. Kruger, P. Liu, Y. R. Fang, and C. R. Appledorn, Med. Phys. **22**, 1605 (1995).

[79] Y. V. Zhulina, Appl. Opt. **39**, 5971 (2000).

[80] R. A. Kruger, D. R. Reinecke, and G. A. Kruger, Med. Phys. **26**, 1832 (1999).

[81] K. P. Kostli, M. Frenz, H. Bebie, and H. P. Weber, Phys. Med. Biol. **46**, 1863 (2001).

[82] M. Xu, and L.-H. Wang, IEEE Trans. Med. Imag. **21**, 814 (2002).

[83] Y. Xu, D. Feng, and L.-H. Wang, IEEE Trans. Med. Imag. **21**, 823 (2002).

[84] Y. Xu, M. Xu, L.-H. Wang, IEEE Trans. Med. Imag. **21**, 829 (2002).

[85] G. J. Diebold, T. Sun, and M. I. Khan, in *Photoacoustic and Photothermal Phenomena III*, edited by D. Bicanic (Springer-Verlag, Berlin, 1992).

[86] V. E. Gusev and A. A. Karabutov, *Laser Optoacoustics*. (AIP, New York, 1993).

[87] M. H. Xu, Yuan Xu and L.-H. V. Wang, IEEE Trans. on Biomed. Eng. **50**, 1086 (2003).

[88] G. Ku, L. -H. Wang, Med. Phys. **28**, 4 (2001).

[89] American National Standard Institue, *American National Standard for the Safe Use of Lasers ANSI Z136.1-2000*, (New York, 2000).

[90] X. Wang, Y. Pang, G. Ku, G. Stoica, and L.-H. Wang, Opt. Lett., **28**, 1739 (2003).

[91] M. Xu and L.-H. Wang, Phys. Rev. E, **67**, 056605 (2003).

[92] A. A. Oraevsky, E. V. Savateeva, S. V. Solomatin, A. A. Karabutov, V. G. Andreev, Z. Gatalica, T. Khamapirad, and P. M. Henrichs, in *Biomedical Optoacoustics III*, A. A. Oraevsky, ed., Proc. SPIE **4618**, 81 (2002).

[93] X. Wang, Y. Pang, G. Ku, X. Xie, G. Stoica, and L.-H. V. Wang, Nat. Biotechnol. **21**, 803 (2003).

[94] X. Wang, G. Ku, M. A. Wegiel, D. J. Bornhop, G. Stoica, L.-H. V. Wang, Opt. Lett. **29**, 730 (2004).

[95] G. Ku, X. Wang, X. Xie, G. Stoica, L.-H. V. Wang, Phys. Med. Biol. **49**, 1329 (2004).

[96] F. Judah, Nat. Med. **1**, 27 (1995).

[97] P. Carmeliet, K. Rakesh, and R. K. Jain, Nature **407**, 249 (2000).

[98] F. Judah, Semin. Oncol. **29**, 15 (2002).

[99] G. D. Hall and G. Stoica, Clin. Exp. Metastas. **12**, 283 (1994).

[100] H. Maeda, Adv. Enzyme Regul. **41**, 189 (2001).

[101] H. Maeda, J. Fang, T. Inutsuka, and Y. Kitamoto, Int. Immunopharmacol. **3**, 319 (2003).

[102] R. G. M. Kolkman, E. Hondebrink, W. Steenbergen, F. F. M. de Mul, IEEE J. Sel. Top. Quantum Electron. **9,** 343 (2003)

[103] A. A. Karabutov, E. V. Savateeva, A. A. Oraevsky, Laser Physics **13**, 711 (2003).

[104] Y.-L. He, H. Tanigami, H. Ueyama, T. Mashimo, and I. Yoshiya, Crit. Care Med. **26**, 1446 (1998).

[105] J. Caesar, S. Shaldon, L. Chiandussi, L. Guevara, and S. Sherlock, Clin. Sci. **21**, 43 (1961).

[106] B. F. Hochheim, Arch. Ophthalmol. **86**, 564 (1971).

[107] M. M. Haglund, M. S. Berger, and D. W. Hochman, Neurosurgery **38**, 308 (1996).

[108] M. L. J. Landsman, G. Kwant, G. A. Mook, W. G. Zijlstra, J. Appl. Physiol. **40**, 575 (1976).

[109] Valery Tuchin, *Tissue Optics* (SPIE, Bellingham, Washington, 2000).

VITA

Geng Ku received his B.S degree and M.S. degree in opto-electronics from Huazhong University of Science and Technology (HUST) (China) in July 1984 and December 1989, respectively. He later joined in HUST as a faculty member. He enrolled in the Ph.D. program in the biomedical engineering department at Texas A&M University in the fall of 2000. The research focused on the development of photoacoustic and thermoacoustic tomography for the biological samples. He received his Ph.D. in biomedical engineering in December 2004.

Geng Ku

233 Zachry Engineering Center

TAMU 3120

College Station, TX 77843-3120